Characterizing and Comparing Tristructural-Isotropic Buffer Properties from AGR-1 and AGR-2 Irradiation Experiments

A Thesis Presented for the
Master of Science
Degree
The University of Tennessee, Knoxville

Austin Tyler Schumacher
December 2019

Copyright © 2019 by Austin T. Schumacher
All rights reserved.

ACKNOWLEDGEMENTS

I owe my deepest gratitude to X-energy for funding this research and allowing me the opportunity to perform this groundbreaking work for my thesis topic. I truly appreciate the opportunity afforded to me through their support. These thanks also extend to the support provided by the Oak Ridge National Laboratory, whose facilities and knowledgeable staff proved vital in performing the following research work. It has also been an honor to study and gain knowledge from the accomplished professors teaching at the University of Tennessee over the course of my master's program.

I would first like to personally thank Dr. Tyler Gerczak for his advice and technical support throughout the process of developing this work. Without his experience and insight none of this work would have likely come to fruition. I also owe a great deal of thanks to my committee members Dr. Stephanie TerMaath and Dr. Reza Abedi for working with me through this process. I am also indebted to my colleagues Dr. Daniel Brown, Dr. Grant Helmreich, Dr. John Hunn, and Brian Jolly who provided a wealth of information regarding past work, technical support, and methods for interpreting data. I could also never forget the help provided by Dr. Maxim Gussev and Dr. Takaaki Koyanagi for their invaluable guidance and support on using equipment critical to this work. Finally, I'd like to acknowledge the hands-on technical work provided by Jesse Werden, Michael Mcalister, Deep Patel, and James Dixon in helping make this work possible.

ABSTRACT

The Advanced Gas Reactor Fuel Development and Qualification program is an ongoing effort to build a database on coated particle fuel for the future licensing and qualification of tristructural-isotropic (TRISO) coated particle fuel production in the United States. Several irradiation experiments have been produced throughout the program, were subjected to irradiation testing, and are currently in the process of post-irradiation examination (PIE). During this examination process it has been found that the first two irradiation experiments displayed varying fracture characteristics of primarily the buffer layer that would affect a particle's ability to retain fission products. This disparity in fracture characteristics is believed to originate from a variation in properties in the particle coatings between the two irradiation experiments. A host of methods for characterizing the primary coating of concern, the buffer, are investigated and ultimately three methods were chosen for testing. Nanoindentation, micro-cantilever testing, and image analysis methods were utilized on particles from both irradiation experiments to identify any variations that may exist between them. Based on the data from nanoindentation and image analysis, differences in both hardness and porosity exist between both irradiation experiments and logically align with why one group of fuel performed differently than the other. The work involving micro-cantilever testing also showed a variation in properties between irradiation experiments that are consistent with why IPyC fractures were more prevalent in AGR-1 but requires more thought in refining the process for more consistent results. The end goal for this work would be to implement a quality control check for testing particle buffer coatings using the methods chosen, but more refining of the methods and testing will be required.

TABLE OF CONTENTS

Chapter One Introduction and General Information 1
1.1 Advanced Gas Reactor Program 1
1.2 TRISO Fuel Particle 2
1.2.1 TRISO Fuel Components 2
1.3 Irradiation and Post-Irradiation Examination 5
1.3.1 AGR-1 7
1.3.2 AGR-2 9
1.4 Qualifying the Buffer and IPyC 11
Chapter Two Literature Review 12
2.1 Pyrolytic Carbon 12
2.2 Physical Testing Methods 14
2.2.1 Nanoindentation 15
2.2.2 Porosity Measurements 18
2.2.3 Micro-Pillar Compression 20
2.2.4 Tensile Specimen 24
2.2.5 Micro-Cantilever Beam Testing 26
Chapter Three Materials and Methods 31
3.1 Overview 31
3.2 Nanoindentation 31
3.2.1 Surrogate Particle Production 31
3.2.2 Sample Polishing and Preparation 32
3.2.3 Keyence Topography Mapping 32
3.2.4 Indentation Methods 34
3.2.5 Nanoindenter Tip Calibration 36
3.2.6 Data Analysis 36
3.3 Tensile Testing 37
3.3.1 Spherical Coating Specimen Preparation 37
3.3.2 Flat Coating Specimen Preparation 39
3.3.3 Tensile Testing 42
3.4 Cantilever Beam Testing 42
3.4.1 Sample Preparation 42
3.4.2 Beam Loading 44
3.5 Image Processing of Porosity 46
Chapter Four Results and Discussion 48
4.1 Nanoindentation 48
4.2 Micro-Cantilever Beam Testing 55
4.3 Porosity Image Analysis 57
Chapter Five Conclusions and Recommendations 65
List of References 67
Vita 72

LIST OF TABLES

Table 1: The results from mapping the surface of 9 particles each polished using different combinations of polishing pads. 35
Table 2: Shows the results of taking the average hardness for the IPyC and buffer for AGR-1 baseline/variant 1 and AGR-2 49
Table 3: The table below shows the minimum hardness values found in the 20 microns of the buffer adjacent to the buffer/IPyC boundary for individual particles. Values in blue are also the absolute minimum hardness values found throughout the buffer 53
Table 4: The table below lists the results for all of the cantilever beams tested per irradiation experiment. Distances for where the beams fractured in relation to the boundary were estimated based on SEM images and corrected for the angle at which the image was taken. 56
Table 5: This table shows the highest porosity percentage band of each particle imaged and the corresponding distance from the boundary within the buffer. The location values refer to the full 1 μm thick band preceding the given value (i.e. 3 refers to all pixels 2-3 μm away from the boundary). 62

LIST OF FIGURES

Figure 1: A cross-section representation of a TRISO coated fuel particle.....3
Figure 2: A stylized illustration of two popular, cross-sectioned fuel compacts composed of TRISO particles, known as prismatic compacts (left) and pebble compacts (right). 3
Figure 3: A cross-section of a furnace used for fluidized bed chemical vapor deposition (Jolly, Lindemer et al. 2015) 4
Figure 4: A cross-section of an irradiation capsule for AGR-1 (Maki 2009). 6
Figure 5: Show a graph shows the release-to-birth ratio of krypton from capsules during the original U.S. TRISO program and the German TRISO program of the 1980s (Petti, Gougar et al. 2005).....8
Figure 6: Shows the tomographic cross-section of two particles that exhibited SiC damage during testing. Spearhead fracture (left) and debond fracture (right) (Hunn, Baldwin et al. 2016).....8
Figure 7: A cross-section of a TRISO particle from AGR-2 that was found to show the worst case of IPyC tearing (Rice, Stempien et al. 2018).....10
Figure 8: (Left) A model illustrating the imperfect graphene sheets found in pyrolytic carbon. Wherein the blue bonds correspond to a hexagonal atomic lattice and the orange bonds correspond to any other bonding structure (Leyssale, Da Costa et al. 2012). (Right) An illustration depicting the microstructure of pyrolytic carbon, where the lines represent the crystallites formed during pyrolysis with soot trapped between them (Ritchie 1996).....13
Figure 9: An illustration showing the various crystallite orientation angles found in pyrolytic carbon and portrayals of how each microstructure may be viewed (Reznik and J Hüttinger 2002). 13
Figure 10: Shows the relationship between displacement into the surface and force applied during a typical loading-unloading cycle of a material undergoing nanoindentation (Oliver and Pharr 1992). 16
Figure 11: (Left) A cross-section of pyrocarbon coated alumina particles. (Right) Shows the hardness results from nanoindentation on pyrocarbon coating produced at varying temperatures (López-Honorato, Meadows et al. 2008). 19
Figure 12: A greyscale micrograph of the porosity found in the OPyC layer by way of SEM imaging (Bari, Osarinmwian et al. 2013).....21
Figure 13: A 3D representation of pores found in the buffer and OPyC produced by XCT shown to the left (Bari, Osarinmwian et al. 2013). While 3D reconstructed images from imaging of the porosity found in a graphite matrix can be found to the right (Arregui-Mena, Edmondson et al. 2018). 21
Figure 14: (Left) SEM images of micro-pillar compression testing specimens after testing occurred (left). (Right) Stress-strain curves produced from the compression of various specimens at different length scales (Uchic and Dimiduk 2005).....23

Figure 15: Shows a FIB-milled micro-pillar with its coating interfaces oriented 55° from the plane normal to compression on the left. To the right shows the resolved stress plot created to determine the interface's internal friction coefficient and debond shear stress (Shih, Katoh et al. 2013).....25
Figure 16: The dimensions specified for the SS-Mini tensile specimen with all dimensions in millimeters (mm). The thickness of the specimen is 0.4mm (Gussev, Howard et al. 2017). 25
Figure 17: An illustration of the steps required to prepare a micron-scale tensile specimen test (Ando, Tanigawa et al. 2018).....27
Figure 18: An SEM image of a notched micro-cantilever beam used in the determination of fracture toughness (Deng and Barnoush 2018). 29
Figure 19: Images of the surrogate TRISO particles used in sample preparation testing. TRISO Surrogate Run 1 is shown on the left and TRISO Surrogate Run 2 is on the right.....33
Figure 20: Shows the particle designation for particles mounted into a hexagonal pattern for use in identifying the locations of indentation schemes. 35
Figure 21: A map of nanoindentation locations and the buffer/IPyC boundary across a surrogate TRISO particle's cross-section produced by way of a Matlab program. Where the red points indicate the indentation locations and the blue line denotes the buffer/IPyC boundary. 38
Figure 22: A model of a tensile specimen with the "ideal" geometry for testing the tensile strength of the buffer. 40
Figure 23: The sample preparation method for producing slabs of epoxy encased TRISO particles for use in tensile testing experiments. 40
Figure 24: The sole dog bone specimen produced for tensile testing of the buffer/IPyC boundary.....40
Figure 25: An image of the tensile specimen produced to determine the weakest coating bond in the TRISO fuel form. The flat coating specimen is wedged between two clear epoxy arms. 41
Figure 26: (Left) An image of the tensile specimen within its mounting apparatus and 3D-printed alignment tool to the left. (Right) The tensile specimen is loaded into an MTS Insight tensile frame on the right. 43
Figure 27: An image of a FIB-produced micro-cantilever beam spanning the buffer and IPyC of a TRISO particle cross-section. The buffer is the porous medium in the top right corner of the image, while the IPyC is the relatively smoother portion throughout the center of the image adjacent to the buffer. 45
Figure 28: The illustration shown above depicts the nanoindenter tip placement when loading the micro-cantilever beams.....45
Figure 29: (Left) A cross-section of a TRISO particle's buffer, IPyC, and SiC with a black line defining the buffer/IPyC boundary can be found on the left. (Right) A black and white threshold image of the same particle. 47
Figure 30: Shows plots displaying the change in hardness in relation to distance from the buffer/IPyC boundary for three particles. Negative values denote

distances within the buffer. Each color corresponds to the results from a different particle. 49
Figure 31: A plot showing the effective filtering achieved by taking the moving average of the hardness as a function of distance from the boundary, where negative values represent points in the buffer and positive points are for indents made inside the IPyC. 51
Figure 32: A plot demonstrating the differences between the nanoindentation results found using a berkovich and a conical tip. 54
Figure 33: The images displayed above show the varying fracture characteristics of three separate micro-cantilever beams. All cantilevers come from AGR-1 variant 1 particles. (Left) Shows a beam that fractured at the base. (Middle) Shows one that has fractured beyond the base. (Right) Shows one that has fractured away from the base. 56
Figure 34: Shows the load required to induce fracture for each of the micro-cantilever beams produced from AGR-1 variant 3 and AGR-2 coatings. 58
Figure 35: An image of a TRISO particle's buffer and IPyC boundary. The porosity imaging code uses three points along this boundary to auto-populate a line assuming the boundary is perfectly circular, but as can be seen this is not always the case. 60
Figure 36: Above shows four separate bar graphs produced from four different TRISO particles subjected to image processing to determine the percentage of porosity found at various distances from the IPyC/buffer boundary. 60
Figure 37: The graph above details the relationship of hardness and porosity within the buffer to the distance from the boundary for an AGR-1 baseline particle. 64
Figure 38: The graph above details the relationship of hardness and porosity within the buffer to the distance from the boundary for an AGR-1 baseline particle. 64

CHAPTER ONE
INTRODUCTION AND GENERAL INFORMATION

1.1 Advanced Gas Reactor Program

The Advanced Gas Reactor Fuel Development and Qualification (AGR) program is a Department of Energy (DOE) initiative led by the Idaho National Laboratory (INL) and coordinated with the help of the Oak Ridge National Laboratory (ORNL). It was created with the intent to build a database for qualifying nuclear fuel in the future licensing and qualification of high temperature gas reactor (HTGR) fuel. This class of reactors is part of the Generation IV initiative aimed at designing reactors and fuel concepts with an array of improved safety, efficiency, and waste reduction characteristics over past generation designs. The HTGR design is unique in the initiative as it is well-suited for the emission-free production of both hydrogen and electricity (Petti, Gougar et al. 2005).

The program entails the fabrication of fuel at the laboratory and industrial scale and the development of quality control methods to ensure the desired fuel properties are attained. The fuel is then loaded into the Advanced Test Reactor (ATR) at INL for irradiation testing so that performance can be evaluated from in-line fission gas release testing and post-irradiation examination (PIE). An array of tests was conducted on seven different fuel production runs known as AGR-1 through AGR-7. Each production run involved the coating of uranium-bearing fuel particles and compaction of said fuel particles into a compact to be used for irradiation testing. AGR-1 was the first production run for the program that focused on testing the fabrication and irradiation methods used in future irradiation experiments. AGR-2 fuel was made with the intent to test two types of uranium-based fuels being produced at a laboratory and industrial-scale. Information on the fabrication process was then used in the production of AGR-3 and AGR-4, which are currently being examined to determine the how well the fuel retains fission products and the transport of these products through graphite in the reactor. Lastly, AGR-5/6/7 are currently under irradiation for use in the qualification of future commercial fuels representing industrial-scale fuel. The AGR-1 PIE has already concluded while examinations of AGR-2/3/4 are currently ongoing. AGR-5/6/7 will be undergoing examination beginning in 2021 (Demkowicz 2017).

1.2 TRISO Fuel Particle

The fuel form chosen for the AGR program is the tristructural-isotropic (TRISO) coated fuel particle. As shown in Figure 1, the TRISO particle consists of a fuel kernel surrounded a porous carbon structure called the buffer, a denser pyrolytic carbon coating called the inner pyrolytic carbon layer (IPyC), a silicon carbide (SiC) coating, and another dense pyrolytic carbon coating called the outer pyrolytic carbon layer (OPyC). The primary purpose of these coatings is to retain the fission products within the structure while the fuel is undergoing fission in a reactor. The TRISO particles are overcoated with a graphite/binder blend and then pressed into the desired fuel compact design. The two styles of compacts utilizing TRISO particles are shown in Figure 2. The first is a prismatic design that takes the form of a right circular cylinder. This form is the compact design chosen for AGR irradiation testing. The second is the pebble design, which is a spherical fuel form. This is the fuel design companies such as X-energy have adopted for production.

The coatings on the TRISO particles are produced by way of fluidized bed chemical vapor deposition (FBCVD). The process involves loading a substrate under some inert gas into a fluidized bed furnace as shown in Figure 3. The inert gas keeps the substrate fluidized while the furnace is heated to a desired temperature. Once the temperature is reached, a precursor gas is introduced that will dissociate at the given temperature resulting in deposition of the desired material onto the substrate. In the case of coating TRISO fuel the spherical fuel kernels act as the substrates for the coatings. Argon is used to fluidize the particles inside the coating chamber and is often mixed with the precursor gases during coating to aid in fluidization. Acetylene (C_2H_2) is the precursor gas for producing the buffer, an acetylene and propylene (C_3H_6) blend is used for producing the pyrolytic carbon layers, while methyltrichlorosilane (CH_3SiCl_3) is bubbled using hydrogen and results in the production of SiC. Altering the deposition conditions such as temperature of the furnace, gas flow rates, and gas fractions will alter the dissociation reactions and therefore the properties of the coatings (Jolly, Lindemer et al. 2015).

1.2.1 TRISO Fuel Components

The core of the particle is a uranium-bearing fuel kernel that measures from approximately 350 to 510 microns (μm) in diameter depending on the fuel variant (Maki 2009, Collin 2011). This kernel either consists of either a low-enriched uranium dioxide (UO_2) or a two-phase uranium dioxide and uranium carbide mixture (UCO) that is produced by a sol-gel process. This kernel provides the fissionable material during reactor operation and therefore is also the source of the gaseous and metallic fission products. The buffer coating that immediately surrounds the kernel consists of a highly porous pyrolytic carbon measuring approximately 100 μm in thickness in the case of AGR fuel (Maki 2009). The purpose of the buffer is to accommodate for the release of fission

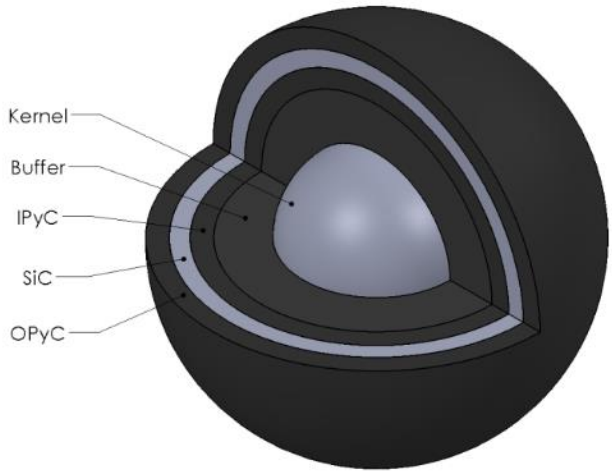


Figure 1: A cross-section representation of a TRISO coated fuel particle



Figure 2: A stylized illustration of two popular, cross-sectioned fuel compacts composed of TRISO particles, known as prismatic compacts (left) and pebble compacts (right).

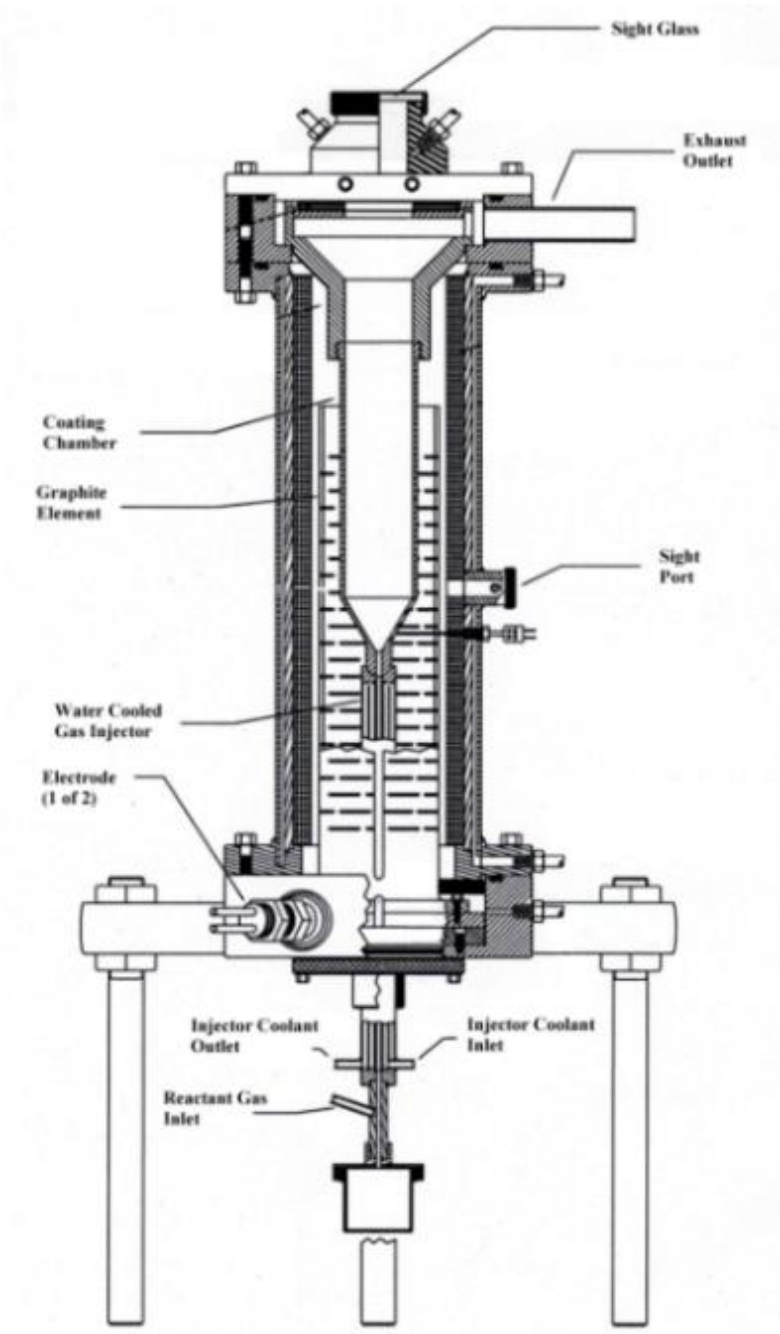


Figure 3: A cross-section of a furnace used for fluidized bed chemical vapor deposition (Jolly, Lindemer et al. 2015)

gases and expansion of the kernel that occurs under irradiation. The IPyC surrounds the buffer and is a higher density carbon coating relative to the buffer (Maki 2009). This layer measures around 40 μm in thickness and has several purposes. The IPyC protects the kernel from hydrochloric acid (HCl) that is a byproduct produced during the deposition of SiC. The coating also helps retain gaseous fission products (such as Kr and Xe) and prevent metallic fission products from interfacing directly with the SiC (Barrachin, Basini et al. 2010). Finally, the IPyC helps add strength to the structure of the overall particle. The silicon carbide coating is 35 μm thick and is the primary structural element of the fuel particle and barrier to the release of metallic fission products. It is necessary for this coating layer to stay intact during the various steps of production and irradiation tests to maintain acceptable fuel performance. The final layer is the OPyC. With similar properties to the IPyC, the OPyC acts as the final barrier for fission product retention in the particle. It also is useful in protecting the SiC layer from external damage.

1.3 Irradiation and Post-Irradiation Examination

The AGR-1 and AGR-2 experiments irradiated prismatic compacts containing anywhere from approximately 1,500 to 4,100 particles depending on the TRISO variant (Maki 2009, Collin 2011). The compacts are loaded into capsules containing instrumentation for online fission gas monitoring capabilities during irradiation. A cross-section of these capsules is shown in Figure 4. The compacts are irradiated at the Advanced Test Reactor (ATR) at INL for approximately two years under varying temperatures, peak burnup, and fast neutron fluence rates (Petti, Gougar et al. 2005, Grover and Petti 2014). Once irradiation testing is complete, the compacts are transported to hot cell facilities at ORNL and INL for PIE.

The primary method for determining the performance of the fuel is particle failure which is indicated by fission product release during irradiation. The release of fission gas from a particle indicates a full coating failure, as any of the pyrocarbon or SiC coatings are capable of retaining these gases. Therefore, during irradiation, either krypton or xenon traps are used to detect whether the sweep gases flowing over the compacts contain fission gases resulting from failed TRISO coatings. However, the release of cesium isotopes, in the absence of krypton and xenon release, from a fuel particle is indicative of whether the SiC coating alone has failed. Therefore, particles with compromised SiC coatings are located by finding where elevated levels of cesium are found in the capsules that housed the compacts during irradiation (Hunn, Baldwin et al. 2016). Once the compacts that exhibited cesium release are located, they are deconsolidated back into discrete TRISO particles and run through the ORNL Irradiated Microsphere Gamma Analyzer (IMGA) to identify the particles that exhibit low

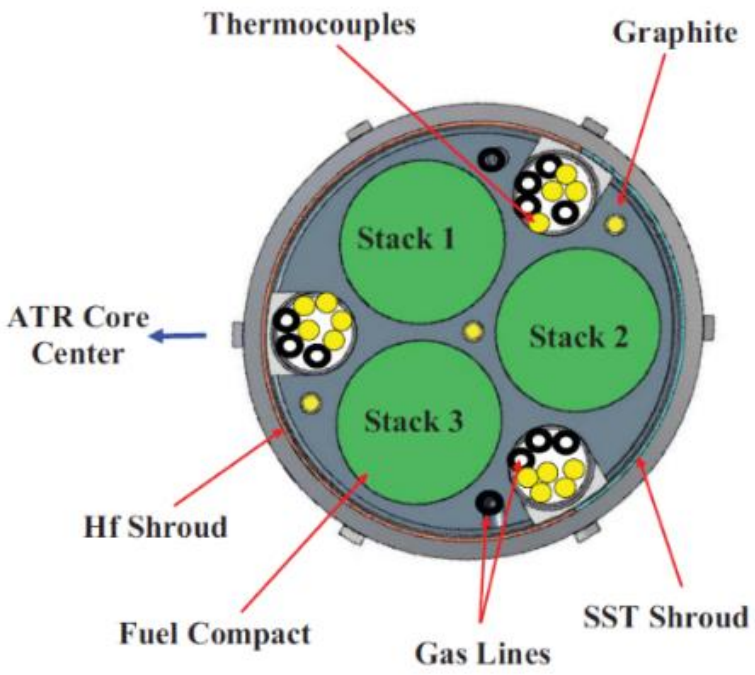


Figure 4: A cross-section of an irradiation capsule for AGR-1 (Maki 2009).

cesium retention and set them aside for further characterization (Hunn, Baldwin et al. 2016).

Safety testing is also a significant effort in the examination process. During safety testing, a few irradiated compacts are exposed to the maximum temperature expected during an accident event at 1600 ˚C and higher (up to 1700 ˚C and 1800 ˚C) to explore margin conditions. This testing mimics what the fission retention performance of the fuels looks like when exposed to accident conditions. The release of fission gases is again tracked using krypton cold traps on the helium sweep gas, while the release of cesium isotopes is accounted for by analysis of a cold trap (which condenses volatiles) found inside the furnace (Hunn, Baldwin et al. 2016).

1.3.1 AGR-1

The first fuel fabrication campaign designated AGR-1 was a laboratory-scale endeavor to refine the fabrication and irradiation methods for subsequent irradiation experiments. The experiment consisted of the four variant production runs, in which various coating conditions were altered. The variants were labelled baseline, variant 1, variant 2, and variant 3. Each variant was composed of multiple coating batches as the coatings were produced in laboratory-scale FBCVD systems. It was compared against the German TRISO fuel produced in the 1980s as it has historically performed orders of magnitude better than past attempts by the US in terms of gaseous fission product retention as shown in Figure 5 (Petti, Buongiorno et al. 2003). Here the fission product retention rate is expressed as the release-to-birth ratio of krypton from a fuel compact. This value represents the ratio of a specific krypton isotope released into the sweep gas from the compacts to the expected total number of krypton atoms produced during irradiation. Once PIE concluded for AGR-1, it was determined that the irradiation experiments succeeded in producing fuel of similar or better quality in terms of gaseous fission product retention than the German fuel the specifications were based on.

The release of cesium during AGR-1 irradiation testing and safety testing indicated compacts containing particles with failed SiC. Out of approximately 298,000 particles irradiated, three particles were recovered that had released cesium during irradiation testing. During safety testing however, three particles were found to have released cesium during 1600 ˚C testing conditions and several more during testing at 1700 ˚C and 1800 ˚C (Hunn, Baldwin et al. 2016). Several of these particles were sorted out by IMGA and the nature of the failures was determined by X-ray tomography. The tomographic slices were used to assist in finding the orientation of the coating damage and obtaining the materialographic cross-section containing the failure to aid in determining the root-cause of failure (Baldwin, Hunn et al. 2014). Figure 6 gives two examples of the type of coating failures found during AGR-1 PIE, being designated spearhead and debond fractures. In both cases, a fracture that began in the buffer

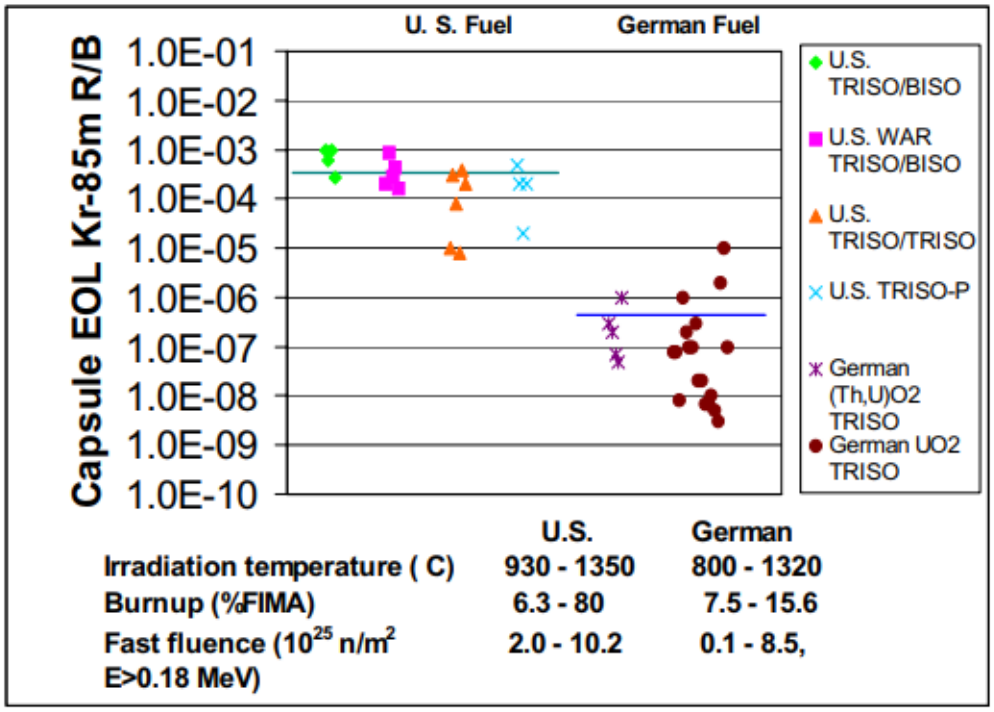


Figure 5: Show a graph shows the release-to-birth ratio of krypton from capsules during the original U.S. TRISO program and the German TRISO program of the 1980s (Petti, Gougar et al. 2005).

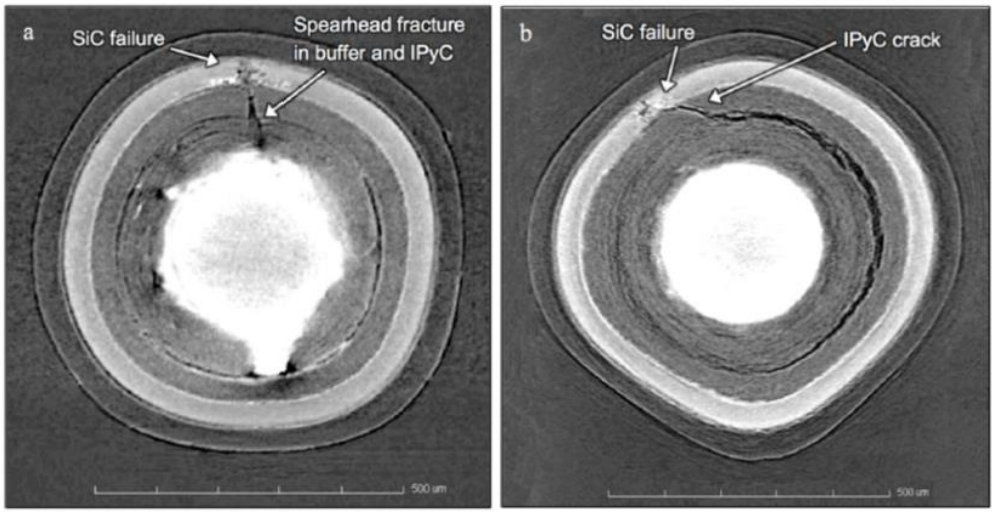


Figure 6: Shows the tomographic cross-section of two particles that exhibited SiC damage during testing. Spearhead fracture (left) and debond fracture (right) (Hunn, Baldwin et al. 2016).

propagated into the IPyC. This crack exposed the SiC to a concentrated attack of metallic fission products (namely palladium) that deteriorated the coating, compromising the particle's ability to retain said fission products (Hunn, Baldwin et al. 2016). In the majority of cases, the densification of the buffer under irradiation would cause it to either partially or fully debond from the IPyC without causing it any damage to the IPyC (Ploger, Demkowicz et al. 2014). This tear typically occurred within the buffer between roughly 0-10 μm from the boundary based on rough measurements taken of particles from compacts 4-4-1, 5-2-3, and 6-1-1 (Hunn, Morris et al. 2012, Hunn, Morris et al. 2013, Hunn, Baldwin et al. 2014). It is therefore speculated that the nature of the buffer and the transition region into the IPyC in these particles influences the fracture propagation into the IPyC.

1.3.2 AGR-2

While AGR-2 did involve the production of two sets of particles with varying kernel chemistry, no coating variants were produced and only one batch of particles were produced since the coatings were deposited at the industrial scale. Irradiation of AGR-2 particles is complete and PIE is ongoing. However, preliminary results have been published on two compacts from the irradiation experiment that have been found to have released cesium during irradiation testing. Once the compacts were deconsolidated, six particles were sorted out by IMGA that were determined to contain low cesium inventories. Out of the six particles observed, one was determined to have been damaged during the fabrication process, two were found to have kernels with naturally low fissionable material, and the remaining three were found to have SiC degradation most likely due to the presence of nickel originating from either the fabrication process or irradiation capsules (Hunn, Baldwin et al. 2018). Therefore, no as-irradiated particles were identified that showed the same SiC failure mechanism that appeared so prevalently in AGR-1 particles.

To get a better idea of how irradiation testing affected AGR-2 coating morphologies, four separate compacts were cross sectioned, polished, and imaged at various planes. Examination of the particles in these compacts showed noticeably different coating fracture characteristics to that of AGR-1, as IPyC tears appeared to be scarcer in these AGR-2 compacts compared to AGR-1 on a percentage basis. Of the few IPyC tears that were found at INL, none made it through the entire coating, with the worst case of a partial tear being shown in Figure 7 (Rice, Stempien et al. 2018). Due to these findings and the data gathered from the failed fuel particles, it is likely that some facet of the AGR-2 buffer and IPyC coatings varies in mechanical properties to its predecessor and contributes to the difference between AGR-1 and AGR-2 buffer fracture characteristics. Other factors could play a role in this variation, such as the difference in kernel size and irradiation conditions that existed between the two

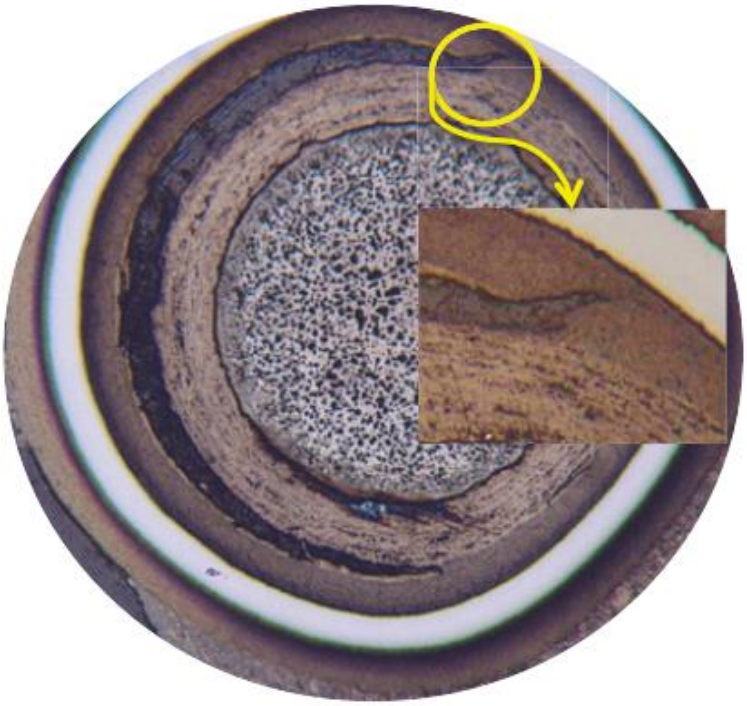


Figure 7: A cross-section of a TRISO particle from AGR-2 that was found to show the worst case of IPyC tearing (Rice, Stempien et al. 2018).

experiments. In this study, however, only the potential differences in the coating properties are investigated.

1.4 Qualifying the Buffer and IPyC

This discrepancy between the buffer/IPyC performance of AGR-1 and AGR-2 isn't fully understood. A current hypothesis being that the longer fluidization time between buffer and IPyC depositions for AGR-2 particles (a consequence of the hot sampling of particles for use in density measurements) results in a weaker interface between the buffer and IPyC (Hunn, Baldwin et al. 2018). Regardless of the reason for why the IPyC tears under irradiation, a method needs to be developed that can differentiate acceptable buffer and IPyC properties. To do this, tests were developed to characterize the buffer and IPyC. Because of the variation in response of the buffer and IPyC to irradiation in AGR-1 and AGR-2, these particles can be used to establish a characterization method and define potential TRISO fuel acceptance criteria. The developed method would result in a metric by which to discern the coatings properties of the two irradiation experiments. This metric could potentially then be used in the future characterization of fuel as a pass/fail criterion or to determine the source of the discrepancy between AGR-1 and AGR-2 coatings. The tests used for characterizing fuel particles must be relatively quick as large batches of material must be tested to get accurate overall statistics on the coating properties for each irradiation experiment.

CHAPTER TWO
LITERATURE REVIEW

2.1 Pyrolytic Carbon

The two primary coating layers to be concerned with (the buffer and IPyC) both consist of a material known as pyrolytic carbon. Pyrolytic carbon is a synthetic carbon structure most commonly produced by the pyrolysis of gaseous hydrocarbons at relatively high temperatures (Kwiecińska and Pusz 2016). Similar to graphite, pyrolytic carbon consists of hexagonal arrays of covalently bonded carbon atoms (graphene layers) stacked on top of one another. Unlike graphite however, the graphene layers are imperfect and not oriented or spaced consistently. During deposition, these imperfect graphene layers form small crystallites on the substrate at various orientations. The dimensions of these crystallites measure around 10 nm in diameter (Ritchie 1996). Therefore, any mechanical test sampling at a sufficiently large enough volume should avoid the anisotropy associated with testing a single crystallite. A model depicting the graphene sheets found in pyrolytic carbon and the formation of graphene crystallites onto a substrate are shown in Figure 8.

Extensive research has gone into characterizing pyrolytic carbon and determining the terminology regarding it. The most common practice for determining PyC microstructure was developed by B. Reznik and K.J. Hüttinger. Their method involves the use of selected area electron diffraction equipment to measure the preferred orientation angle (OA) of the specimen. Four different levels of preferred orientation were defined and given terms. They are designated isotropic, low textured, medium textured, and high textured, with the preferred orientation of the crystallites increasing with each type starting with isotropic structure (Reznik and J Hüttinger 2002). An illustration of these structures is shown in Figure 9. While this terminology is commonly used as the basis for defining PyC microstructures, other methods exist to determine a sample's anisotropy. The AGR program measures the optical anisotropy factor (OAF) in the coatings by way of a two-modulator generalized ellipsometer microscope (2-MGEM). The OAF is a ratio of the maximum reflectivity at a location to the minimum reflectivity at the same location. The 2-MGEM measures the diattenuation of the specimen at various points and export a map of these values across the surface of the sample. Diattenuation is the measurement of a material's ability to absorb polarized light differently along two orthogonal axes. The diattenuation value can then be directly correlated to the OAF for the coatings using Equation 1(Jellison and Hunn 2008).

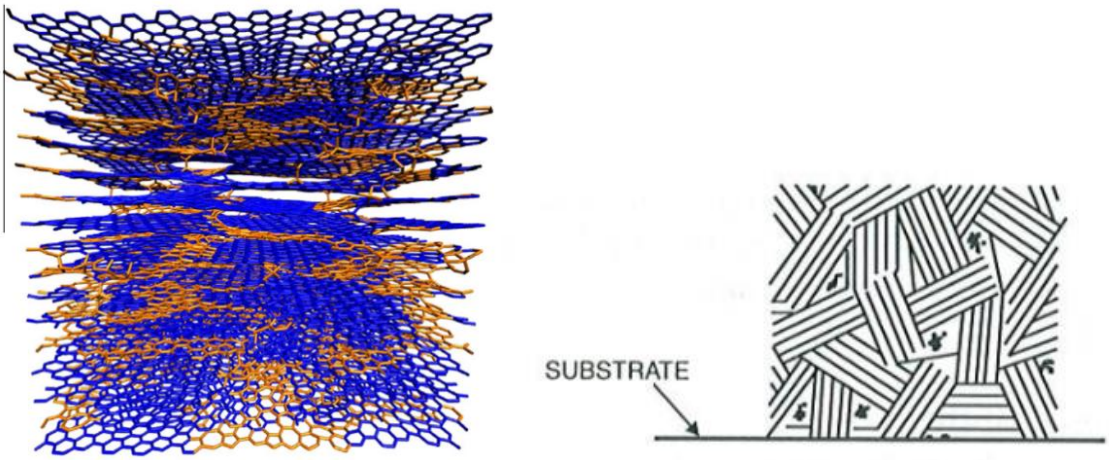


Figure 8: (Left) A model illustrating the imperfect graphene sheets found in pyrolytic carbon. Wherein the blue bonds correspond to a hexagonal atomic lattice and the orange bonds correspond to any other bonding structure (Leyssale, Da Costa et al. 2012). (Right) An illustration depicting the microstructure of pyrolytic carbon, where the lines represent the crystallites formed during pyrolysis with soot trapped between them (Ritchie 1996).

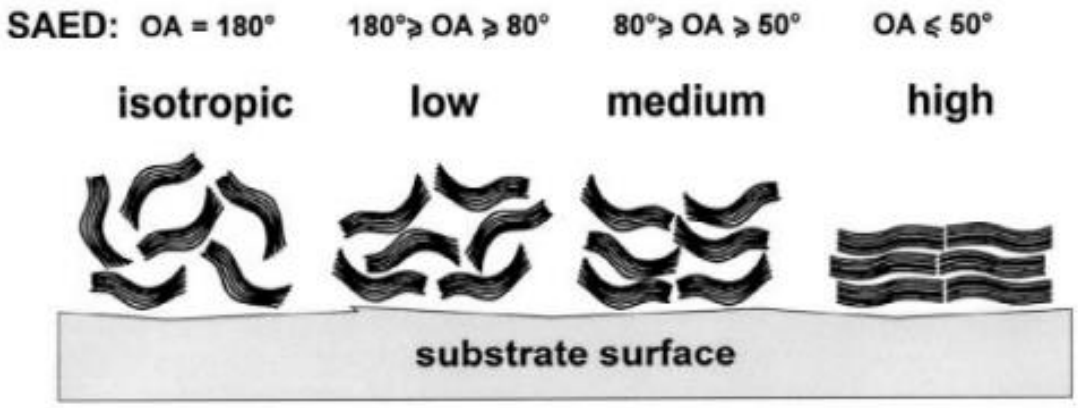


Figure 9: An illustration showing the various crystallite orientation angles found in pyrolytic carbon and portrayals of how each microstructure may be viewed (Reznik and J Hüttinger 2002).

Equation 1: $$OAF = \frac{1+N}{1-N} \sim 1 + 2N$$

In this equation N is the diattenuation of the sample. The anisotropy factors for AGR-1 and AGR-2 IPyC coatings were found to be relatively low (<1.035 OAF) (Maki 2009, Collin 2011). Buffer diattenuation values overall were found to be lower than that of the IPyC. This is linked to the finding that faster deposition rates generally correspond to lower diattenuation values and therefore lower anisotropy (Lowden, Hunn et al. 2005). These low anisotropy values in the coatings will allow for the measurement of mechanical properties with negligible effects from preferred crystallite orientations.

Buffer and IPyC coatings both contain pores, but visually between the two coatings a stark contrast in their porosities can be noticed. While their porosities most likely do not contribute fully to the deviation in their densities from theoretical density, it is likely the main contributor. Therefore, a metric available for comparing the porosities would be their percentages of theoretical density. Using the AGR-1 coating density target, this results in an approximately 42% dense buffer and 84% dense IPyC (Maki 2009) when compared to the theoretical density of graphite at 2.26 g/cm^3. Further investigation into the porosities of the pyrolytic carbon coatings has been a limited field of research since pore morphology has not shown itself to be a fundamental concern in fuel fabrication. Much of the work quantifying the porosity are typically performed by way of mercury intrusion measurement methods (Lowden, Hunn et al. 2005, López-Honorato, Meadows et al. 2008). Since porosity can play a large factor into the behavior of mechanical testing specimens (Phani and Niyogi 1987, Chen, Nagao et al. 2017) these overall porosities and pore sizes must be considered when determining which tests to perform and how to dimension the resulting specimens.

2.2 Physical Testing Methods

Any test performed would be done to find any discrepancies that exist between buffer and possibly IPyC coatings between the two irradiation experiments. Several methods for characterizing the coating layers were investigated in preparation for this work. Most of the physical testing methods revolve around micro-mechanical testing or various techniques for imaging the fuel since the scale of the coatings is on the order of microns. With regards to micro-mechanical testing however, the specimen sizes must be large enough so that the test is representative of the bulk properties of a single TRISO particle and the tests must be performed on enough specimens as to create an accurate statistical representation of the irradiation experiment's coating properties. Since the end goal of this study would be to develop a quality control check for particle fuel coatings at an industrial-scale, the methods are also weighed on their

viability for testing a number of samples necessary for a production facility setting.

2.2.1 Nanoindentation

Nanoindentation is a form of mechanical testing developed for measuring the hardness and elastic modulus of small volumes and thin films. It is a popular method known for its relatively quick ability to probe mechanical properties and uncomplicated sample preparation requirements. The equipment typically utilizes a diamond tip indenter with a well-defined geometry to make indents into a given sample. These tips can take various shapes such as the common three-sided berkovich tip, the four-sided Vickers tip, or the cono-spherical tip. These tips are pressed into the material in question while the displacement into the sample and force applied are monitored throughout the loading and unloading process. An image of the typical force-displacement curve produced by one of these tests is shown in Figure 10. The hardness is then found using the following equation. Where H is the value for hardness, P is the load applied, and A is the projected area of the indenter tip at the given depth into the indentation.

Equation 2: $$H = \frac{P}{A}$$

As opposed to traditional indentation methods, measuring the indentation left by nanoindenters is neither a simple nor quick process. Due to this, it is most common to characterize the geometry of the tip through various means to produce an equation that will accurately predict the projected area of a tip as a function of the indentation depth. This area equation follows the form shown below for all tip geometries.

Equation 3: $$A(h_c) = c_0 h_c^2 + c_1 h_c + c_2 h_c^{1/2} + \cdots + c_n h_c^{2/2^n}$$

In this equation h_c is the depth of the indentation into the sample and c_n are the area coefficients for the best fit line that corresponds to the actual depth to projected area relationship of the tip. For a perfectly sharp tip with no rounding only the first term is required in most cases. However, it is impossible to sharpen a tip to a perfect point and therefore all tips will exhibit rounding to some extent or exhibit some sort of geometric irregularities. Therefore, the supplemental terms are added to suit the indenter geometry.

The elastic modulus of a material may also be calculated given data from a nanoindentation test. If one knows the Poisson's ratio and elastic modulus for the indenter material (υ_i and E_i respectively), the Poisson's ratio for the material being indented (υ), and the reduced elastic modulus (E_i) then the elastic modulus for the material can be found using a common contact mechanics equation as shown in Equation 4 (Oliver and Pharr 1992).

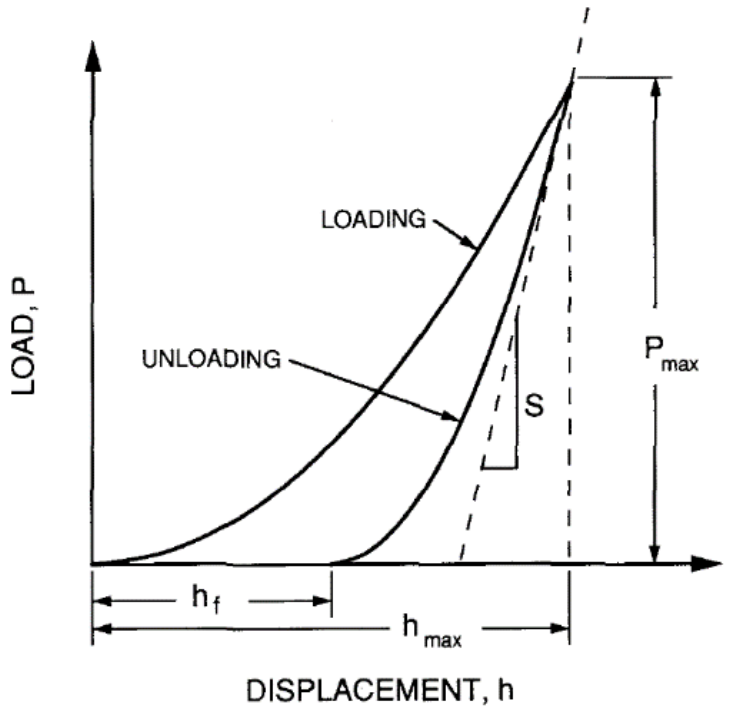


Figure 10: Shows the relationship between displacement into the surface and force applied during a typical loading-unloading cycle of a material undergoing nanoindentation (Oliver and Pharr 1992).

Equation 4: $$\frac{1}{E_r} = \frac{1-\upsilon^2}{E} + \frac{1-\upsilon_i^2}{E_i}$$

To find the reduced modulus of the system used to solve this equation, the stiffness (S) of the material must first be calculated. Two methods exist for calculating this stiffness: the unloading method and the continuous stiffness measurement (CSM) method. The unloading method involves fitting the unloading curve of the indentation to an exponential equation and finding the slope at the exact point where the unloading begins (Oliver and Pharr 1992). This slope is the stiffness of the system. In the case of the CSM method, a small harmonic load is imposed on the sample during loading. The reaction of the displacement to the imposed force by way of the phase angle between the two can be used to determine the stiffness of the system continuously throughout the loading cycle (Li and Bhushan 2002). The stiffness values calculated by way of these two methods can then be plugged into the following equation which relates stiffness to the system's reduced modulus (Oliver and Pharr 1992). In this equation β is a constant that accounts for the shape of the indenter.

Equation 5: $$E_r = \frac{\sqrt{\pi}}{2\beta}\frac{S}{\sqrt{A}}$$

One obstacle in the nanoindentation process is accurately obtaining area function coefficients representative of the tip geometry. International Standard 14577 was written to guide a user through the nanoindentation process and help ensure accurate and repeatable testing methods. This standard contains calibration procedures for an array of processes, including recommendations for the calibration of the indenter tip area function. Three general methods are recommended for this process: mapping the topography of the tip directly with an atomic force microscope (AFM), indenting into a material with a well-defined modulus of elasticity, or indenting into a material with a well-defined hardness value (Fischer-Cripps 2011). No matter which method is chosen some level of analysis is required to retrieve characteristic area function coefficients. For mapping the surface, the topography map must be analyzed to determine the area at varying depths, which must be used to create a best fit line for the area function (VanLandingham, Juliano et al. 2005). However, software already exists for reverse engineering the area coefficients that comes from indenting into a material with a known modulus as it is the most common method. Calibration using a reference material with a known hardness is the least common method, but procedures have been developed (Schiffmann 2007).

Since the integrity of the TRISO fuel particle is of primary concern when evaluating fuel performance, the coating layers have previously undergone some level of mechanical testing. Many of these tests have been focused on characterizing the properties of the SiC (Hosemann, Martos et al. 2013) as it is the most important coating layer in terms of fission product retention. But investigations into the mechanical properties of pyrocarbon have also been

performed, including nanoindentation testing (Bellan and Dhers 2004, López-Honorato, Meadows et al. 2008, Gross, Timoshchuk et al. 2013)

Work performed by Bellan and Dhers investigated the evaluation of elastic modulus for SiC and PyC for use in modelling the performance of the fuel. Several methods were utilized including nanoindentation, acoustic microscopy, and impulse excitation method. Specimens were produced by way of FBCVD of pyrocarbon and SiC onto flat substrates. The coatings were mechanically polished and a series of nanoindentations were performed on each specimen at various points to test reproducibility. Testing showed that the elastic modulus for the pyrocarbon specimens averaged out to 25.5±2 GPa. This value was found to be comparable to the modulus value found by way of impulse excitation method, which was found to be between 28.9 and 30.8 GPa. From the PyC and SiC indentation results the authors came to the conclusion that while nanoindentation may not have been the most accurate method for determining elastic modulus, it is highly reproducible and simple to perform (Bellan and Dhers 2004).

An investigation into the effects of pyrocarbon coating conditions were performed in hopes of determining how these factors play a part in regulating mechanical properties. The testing method involved characterizing samples by way of nanoindentation, Raman spectroscopy, microscopy, and porosimetry. As opposed to the work previously mentioned, this work focused on characterizing the coatings produced on spherical surrogate kernels. This was to avoid any discrepancies that may arise from the coating of flat substrates as they will fluidize differently during the FBCVD process. Alumina beads were coated in a FBCVD furnace under various run conditions such as gas concentration, furnace temperature, and gas composition. The surrogate particles were then cross-sectioned and polished to half plane so that nanoindentations could be performed on a flat surface. A cross-section of these surrogate particles and some of the load-displacement curves from testing are shown in Figure 11. The results showed that the elastic modulus and hardness both decreased with increase in temperature for both acetylene and acetylene/propylene-derived pyrocarbon. When comparing the effects of coating conditions on the density and porosity measurements to the nanoindentations results, it was found that in some cases the change in density wouldn’t correlate to a change in mechanical properties. From this it was reasoned that other factors must play a part in determining the mechanical properties of the PyC outside of the just porosity and density (López-Honorato, Meadows et al. 2008).

2.2.2 Porosity Measurements

Characterization of the porosity between AGR-1 and AGR-2 pyrocarbon coatings was also considered upon recognizing that the tears in the coatings typically occurred in a band of the buffer with a visibly high porosity. Therefore, several methods defining the morphology of the pores near the interfacial region were investigated. The first testing method considered is related to the

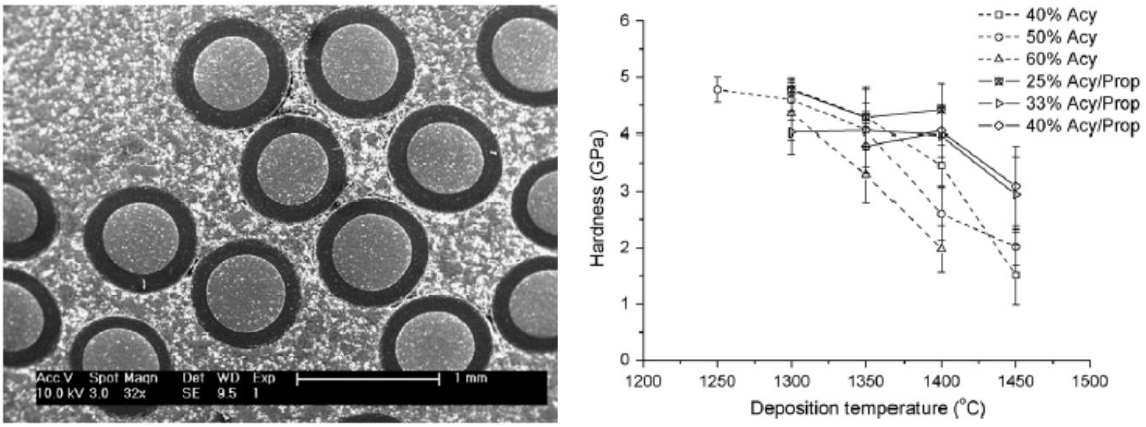


Figure 11: (Left) A cross-section of pyrocarbon coated alumina particles. (Right) Shows the hardness results from nanoindentation on pyrocarbon coating produced at varying temperatures (López-Honorato, Meadows et al. 2008).

examination technique used to define the voids found in the fuel kernels (Helmreich, Hunn et al. 2018) and has been utilized in various other studies (Spierings, Schneider et al. 2011, Lowe, Bradley et al. 2015, Lima Neto, Ceia et al. 2018). In this experiment 2D images are taken of the sample cross-section by way of an optical microscope or scanning electron microscope (SEM). These cross sections are then then put through an image analysis program in which the images are converted into greyscale. In the micrographs produced, the darkest pixels in the images typically correspond to pores as the light from optical microscopy or the electrons from an SEM diffuse upon interaction with them. Figure 12 shows the porosity found in the OPyC using this method. The aforementioned image processing software can then determine the porosity characteristics by analyzing the pixel bit values (Bari, Osarinmwian et al. 2013). This form of analysis is relatively quick compared to some other methods since the analysis is automated and the only sample preparation required is cross-sectioning and polishing. The issue in this examination process comes from the error associated with characterizing a 3D pore as a 2D cross-section since any given pore's morphology will change with depth. One way of rectifying this issue is to image the porosity in three dimensions. Past research has identified a few methods to accomplish this task (Bari, Osarinmwian et al. 2013, Arregui-Mena, Edmondson et al. 2018). The first method involves utilizing X-ray computed tomography (XCT) to take 2D images of the specimen at varying depths to create a 3D representation of the target. The porosity characteristics can then be extracted from this model to obtain more representative values than would be obtained from 2D image analysis. The second method works similarly in that several 2D images are compiled into a 3D map of the sample, but the map is produced after physically removing material to image the porosity at varying depths. The removal of material could be achieved by either focused-ion beam (FIB) milling (Arregui-Mena, Edmondson et al. 2018) or by polishing a cross-section at specified intervals. While both of these approaches work in much the same way, the XCT available for this work has a noticeably lower resolution on the order of 1 μm and the slice and view method can be time-consuming depending on the methodology chosen. Examples of 3D reconstructed images of porous materials using both techniques are shown in Figure 13. These approaches could be tested alongside one another to obtain a complete picture of the pore morphology. Other well-known methods for measuring macro-porosity such as helium pycnometry and mercury intrusion are also viable options to include in characterization (Bari, Osarinmwian et al. 2013).

2.2.3 Micro-Pillar Compression

One popular method for measuring the bonding strength of an interface at the micron-scale would be the application of micro-pillar compression testing. The use of creating micro-fabricated pillars for use in uniaxial compression

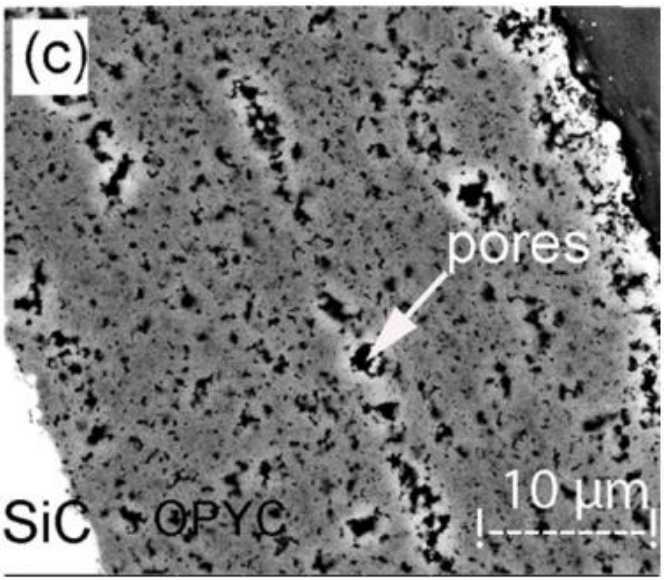


Figure 12: A greyscale micrograph of the porosity found in the OPyC layer by way of SEM imaging (Bari, Osarinmwian et al. 2013).

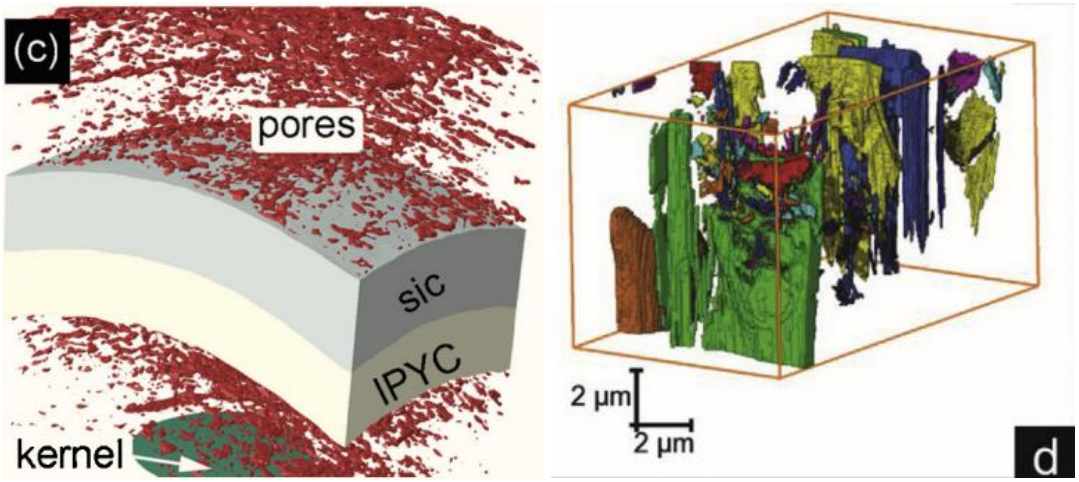


Figure 13: A 3D representation of pores found in the buffer and OPyC produced by XCT shown to the left (Bari, Osarinmwian et al. 2013). While 3D reconstructed images from imaging of the porosity found in a graphite matrix can be found to the right (Arregui-Mena, Edmondson et al. 2018).

testing came from a desire to test the size effects of crystalline materials (Uchic and Dimiduk 2005). In the work of Uchic and Dimiduk, small cylindrical specimens of various diameter and height were fabricated out of a single-crystal Ni superalloy using FIB milling. The micro-pillars produced during this experiment were then loaded into a nanoindenter that is outfitted with a flat, diamond indentation tip to act as a platen for the compression test. With the indenter under displacement control, the pillars were uniaxially compressed with the load and displacement recorded throughout for each of the samples. Images of the resulting compression tests and the stress-strain curves generated from them are shown in Figure 14. The results from the testing were able to show consistent flow stress results at 3% strain for samples wider than 10 μm in diameter and considerable size effects for samples at smaller length scales (Uchic and Dimiduk 2005).

Different techniques were also utilized to produce these geometries as milling larger specimens with a FIB can require an infeasible amount of time. These methods included micro-electrodischarge machining (micro-EDM) and laser ablation, both of which are orders of magnitude faster at removing the same volume of material albeit with less precision. The authors also went on to produce sample geometries that are used in other common macro-mechanical tests as a proof of concept for future micro-mechanical testing methods such as dog bone specimens for use in micro-tensile testing. Since these initial tests, micro-pillar compression tests have been used for an array of experiments with the intent of determining material characteristics at the micron and sub-micron scale (Yilmaz, Jelitto et al. 2015, Kurdi and Basak 2018, Zhao, Guo et al. 2018).

In work performed by Shih, Katoh et al. the use of micro-pillar compression testing had been modified to characterize the interface properties of a ceramic matrix composite. A SiC fiber was coated with five alternating 50nm thick pyrocarbon and five 1 μm thick SiC layers. These coated fibers were then FIB milled into multiple micro-pillars with the coating interfaces at various orientations to the plane normal to the compression axis. Since some metric was required to measure the strength of the coating interfaces, a brittle failure criterion was needed that would accurately represent the mode in which the pillars failed. The Coulomb-Mohr fracture criterion that is generally applied to the shear fracture of rock surfaces (Handin 1969) was chosen to estimate the interface debond shear stress and internal friction coefficient. This model uses fracture load (P_{break}), the cross-sectional area of the pillar (A), the angle of the interface in relation to the plane normal to the axis of compression (θ), the coefficient of internal friction (μ), and the shear debond stress of the interface (τ_{debond}) in the following equation (Shih, Katoh et al. 2013).

Equation 6:
$$P_{break} \cdot \frac{\sin\theta \cdot \cos\theta}{A} = \tau_{debond} + P_{break} \cdot \frac{\cos\theta \cdot \cos\theta}{A} \cdot \mu$$

Creating specimens with varying values for the angle of the interface should fit this equation well so long as the fracture criteria holds true for the given

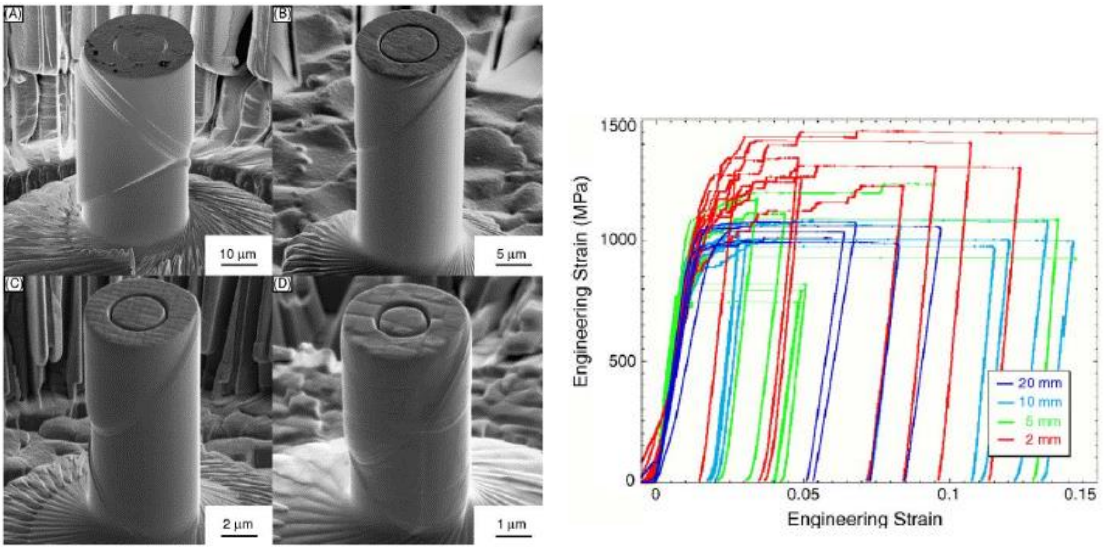


Figure 14: (Left) SEM images of micro-pillar compression testing specimens after testing occurred (left). (Right) Stress-strain curves produced from the compression of various specimens at different length scales (Uchic and Dimiduk 2005).

material interface. The best fit line for these test results will then give the debond shear stress value and internal friction coefficient for a material's interface. Three interface angles were used to verify that the interface follows the best fit line in this case. Figure 15 shows an example of one of these micro-pillar samples with an interface angle of 55° and the best fit line produced by the results from these micro-pillar compression experiments (Shih, Katoh et al. 2013).

In terms of applying this approach to TRISO coatings, the region of the buffer that is tearing during irradiation testing could be treated as the debonding interface oriented at varying angles. However, in using this method there is no guarantee that the buffer would fracture the way as predicted by this method seeing as there isn't a distinct interface. There is also an issue with the effort required to produce FIB-fabricated specimens as milling away the necessary material can be time-consuming for producing a meaningful number of samples.

2.2.4 Tensile Specimen

When investigating the primary cause of debonding failures found in AGR-1, it can be surmised that the buffer in most cases densified and attempted to pull away from the IPyC while under irradiation. Therefore, a direct measurement of the tensile strength for the buffer would be most relevant method for characterizing its mechanical properties. Nevertheless, conducting tensile tests with coatings that are tens of microns thick presents a few logistical issues such as how to produce such specimens and how to test them. Two distinct methods have been reviewed that pertain to tensile testing at differing length scales.

Methods for creating and testing relatively small tensile specimens have already been investigated at ORNL in the hopes of reducing the cost of irradiation tests for metals. Past irradiation studies at the lab had utilized a geometry known as the SS-J type specimen, but the need for less substantial samples lead to the design of the SS-Mini. This need to produce less substantial specimens is the result of the limited space for irradiation testing inside of a reactor and the desire to limit the dose rates produced by irradiated specimens. The study examined whether size effects occurred in various commercially available metals for this new design and which features resulted in the yield stresses and elongation values closer to those found by experimentation with the larger SS-J specimens (Gussev, Howard et al. 2017). The resulting tensile specimen design for the SS-Mini can be seen in Figure 16, where the thickness comes out to be 0.4mm. While the grain size of the metals being tested was the primary factor in determining the cross-sectional thickness of the design (Gussev, Howard et al. 2017), the dimensions of the TRISO coatings are the limiting factor in creating a suitable specimen design. Therefore, a modification to the dimensions of the SS-Mini design would be made, but the testing apparatus consisting of a tensile frame and strain measurements utilizing Digital Image Correlation (DIC) would still be viable. Another issue stemming from the

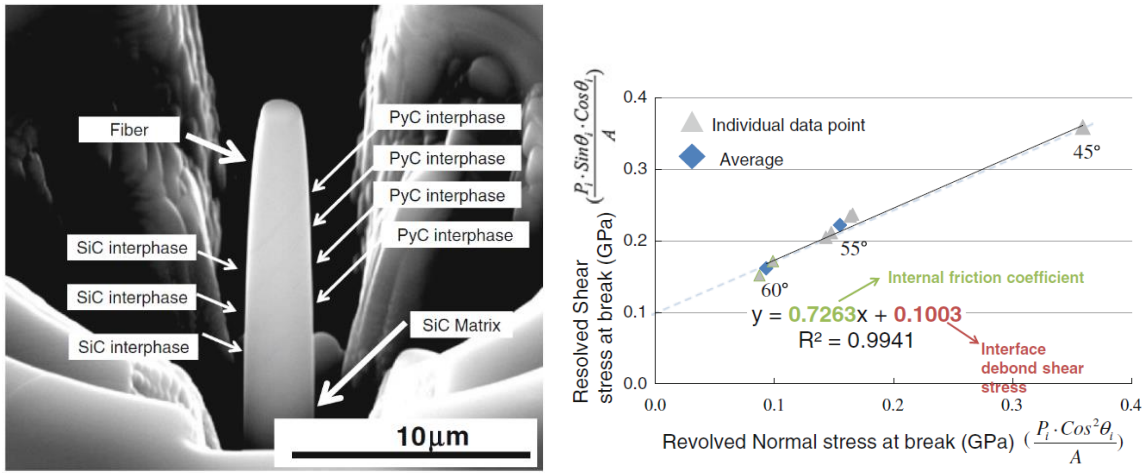


Figure 15: Shows a FIB-milled micro-pillar with its coating interfaces oriented 55° from the plane normal to compression on the left. To the right shows the resolved stress plot created to determine the interface's internal friction coefficient and debond shear stress (Shih, Katoh et al. 2013).

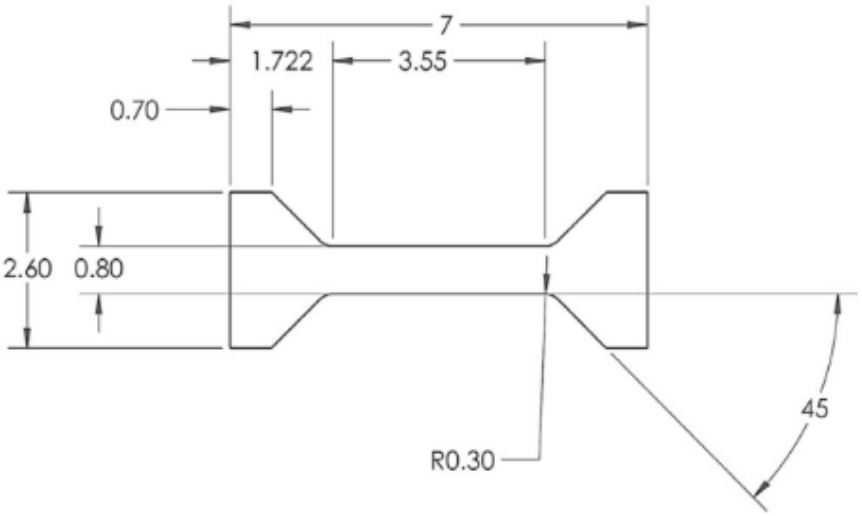


Figure 16: The dimensions specified for the SS-Mini tensile specimen with all dimensions in millimeters (mm). The thickness of the specimen is 0.4mm (Gussev, Howard et al. 2017).

dimensions would be the fabrication of a part with such a diminutive cross-section without destroying it.

Akin to the micro-pillar compression testing methods, micro-tensile tests have been performed to some extent (Huang, Huang et al. 2005, Ando, Tanigawa et al. 2018). Compared to most of the other micro-mechanical testing methods investigated, micro-tensile testing is the most logistically complicated for an assortment of reasons. The main concerns for performing micro-tensile tests stems from grasping and actuating the specimen. These issues were addressed in an attempt to characterize the mechanical properties of irradiated reduced activation ferritic/martensitic (RAMF) steels. In this study, tensile specimens of neutron irradiated and non-irradiated RAMF steels were produced at the micron scale and compared to specimens prepared at the millimeter scale to investigate the effects of irradiation on mechanical properties. The specimens were produced by way of FIB milling and resulted in a gauge section approximately 1 μm thick and 1 μm wide. One end of these specimens is bonded to a SiC base that has been milled into a fixed beam geometry. The other end has a tungsten tip (commonly used in TEM sample lift-out) fused to the top end of the specimen by way of tungsten deposition. This tungsten needle is then attached to an actuator that ensures motion in the axial direction only. When the tungsten needle pulls on the specimen, the deflection of the SiC fixed beam is tracked and used to estimate the load pulling on the specimen (Ando, Tanigawa et al. 2018). An illustration of the fabrication process is displayed in Figure 17. The results of this experiment were compared against the results found from tensile tests of the same materials utilizing the SS-3 specimen geometry. In general, the yield and ultimate strength results between the two experiments did not match up well due to various size effects discussed in the study. However, the tests did display the same trend in the irradiation hardening effect in the RAMF steels. This experiment demonstrates that this method can accurately mimic the differences found in the tensile testing process at the millimeter-scale. However, similar to the micro-pillar compression testing method, the FIB milling of these dog bone specimens would require an extensive amount of time to produce. The method is also relatively new and untested compared to a few of the other experiments investigated and therefore may require validation or refinement by additional sources.

2.2.5 Micro-Cantilever Beam Testing

The final micro-mechanical testing method that will be examined is the micro-cantilever mechanical test. Similar to the micro-pillar and micro-tensile tests, the micro-cantilever method is essentially a scaled-down version of a typical cantilever beam bending test that relies on the same basic beam theory principals as its macroscopic counterpart. This technique has been adopted by many researchers in the determination of mechanical properties for an array of

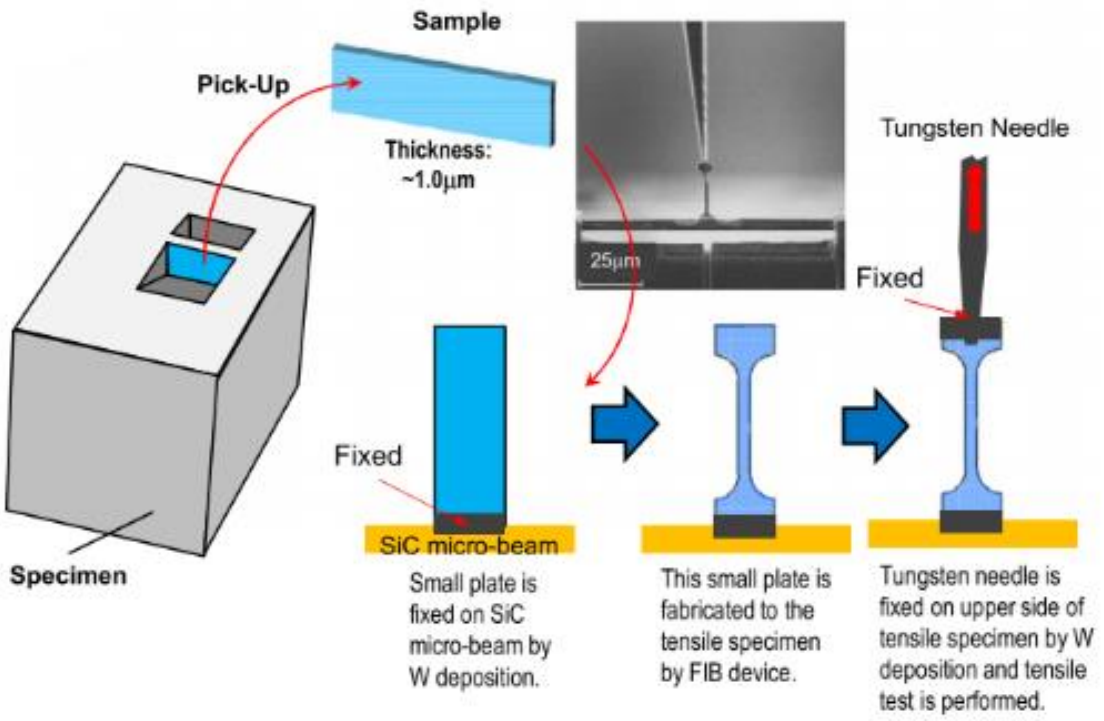


Figure 17: An illustration of the steps required to prepare a micron-scale tensile specimen test (Ando, Tanigawa et al. 2018).

materials (Weihs, Hong et al. 2011, Armstrong, Hardie et al. 2015, Liu and Flewitt 2017). The utilization of micro-cantilevers in mechanical testing came from a need to characterize the properties of thin films while overcoming the issues associated with various other micro-mechanical testing methods at the time. The experiments involved depositing patterns of silica (SiO_2), low temperature oxides (LTO), and gold (Au) thin films onto silicon substrates. The silicon was then chemically etched away to expose the free-standing thin film beams. A nanoindenter was then used to load the cantilever beams for testing. This experiment allowed for the determination of the yield strength and elastic modulus of the beams given the load-displacement data from the nanoindentations. The mechanical properties of all three materials showed agreement with results found using other thin film measurement techniques (Weihs, Hong et al. 2011).

The milling of micro-cantilevers for use in micro-mechanical testing has developed greatly since those initial tests. The advancements in SEM technology and the proliferation of FIB fabrication methods have allowed for the accurate testing of several materials at the micron scale (Matoy, Schönherr et al. 2009, Armstrong, Hardie et al. 2015, Liu and Flewitt 2017). Using the same basic methods for fabricating these cantilever specimens, techniques have been developed for determining the fracture toughness of a given material by introducing a pre-crack to the beam (Di Maio and Roberts 2005, Chen, Nagao et al. 2017, Deng and Barnoush 2018). These fracture testing specimens most commonly take the form as shown in Figure 18. Where the beam has a rectangular cross-section and a notch is milled near the base of the beam to induce cracking under load. The beam is placed under load by way of nanoindentation similarly to the standard cantilever test and the load at fracture is extracted. Many of the materials that are examined using this method are brittle (Žagar, Pejchal et al. 2016) and undergo negligible plastic deformation, so linear elastic fracture mechanics (LEFM) derived stress intensity factor (SIF) equations are often used (Matoy, Schönherr et al. 2009, Deng and Barnoush 2018). These equations take the following form.

Equation 7: $$K_{1C} = f\left(\frac{a}{w}\right)\sigma_C\sqrt{\pi a}$$

The critical stress, σ_C, is a function of the critical load on the specimen and the geometry being utilized for testing. The equation for this stress can be found in SIF handbooks. The value K_{1C} is the SIF at the structure's critical load, which is equivalent to the fracture toughness. The function f(a/w) is a nondimensional correction factor that takes the geometry of the specimen into account. The correction factor for some geometries will be located in SIF handbooks, but often needs to be determined for a specific set of dimensions using finite element models (FEM). Lastly α is the depth of the crack into the specimen. Inputting the critical load found using nanoindentation into the aforementioned equation will output the material's fracture toughness.

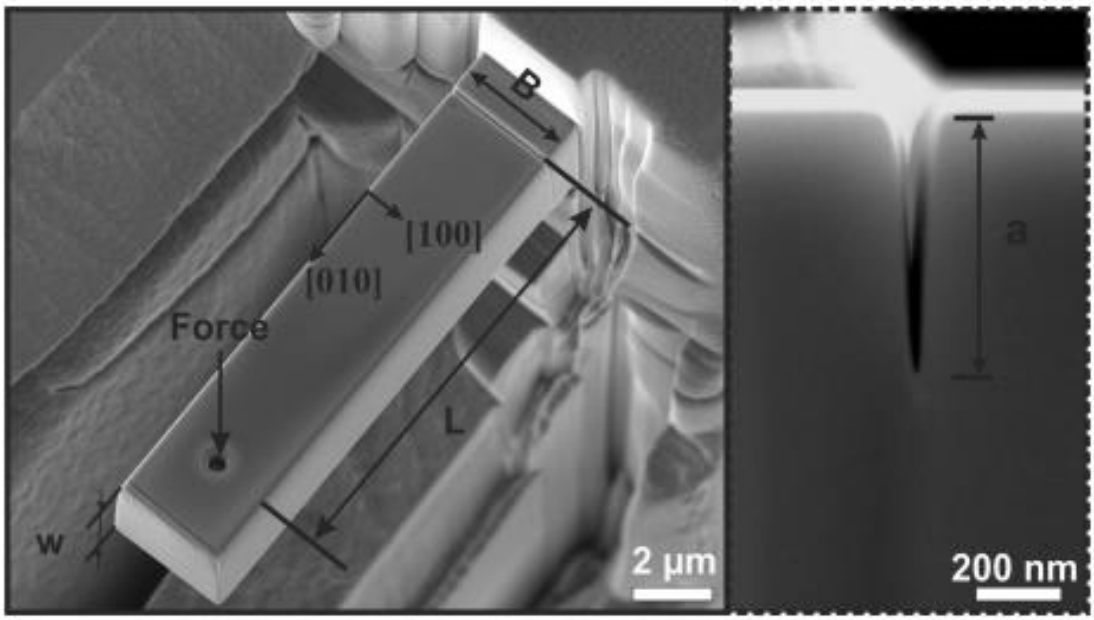


Figure 18: An SEM image of a notched micro-cantilever beam used in the determination of fracture toughness (Deng and Barnoush 2018).

When it comes to the process of milling these specimens, one critical issue becomes apparent in the fabrication process. It is that milling 3-dimensional beams from a planar specimen proves an arduous task if the sample is not already near an edge, as the underside of the beam must be free-standing. This difficulty can be overcome by undercutting the beams at angles to produce either a pentagonal or triangular cross-section as found in many micro-cantilever studies (Di Maio and Roberts 2005, Armstrong, Hardie et al. 2015, Žagar, Pejchal et al. 2016). This however, either limits the number of samples available for milling to the number that can fit near an edge or results in extensive FIB time allotted for milling out cantilever beam specimens.

CHAPTER THREE
MATERIALS AND METHODS

3.1 Overview

Three methods were chosen for mechanically testing AGR-1 and AGR-2 buffer and IPyC coatings. Nanoindentation was determined to be a convenient method for its capability to rapidly probe the mechanical properties across the coating boundary and the lack of complex preparation methods required to produce suitable samples for testing. However, seeing as the buffer/IPyC coatings fracture in tension during irradiation testing, an approach resulting in the fracture of the coatings by way of tensile stresses was desired. Since nanoindentation testing does not result in the aforementioned type of failure, a second method was selected that would. Originally tensile testing experiments were selected for the second technique due to its direct measurement of the coating's strength in tension. However, complications in the fabrication process of specimens and coating bonding characteristics became apparent, so another process was elected in its place. It was then decided that performing micro-cantilever bending tests were a suitable alternative to pursue. The beams would be tested to determine the flexural strength of the buffer instead of the fracture toughness as fracture toughness calculations would require finite element modelling to calculate an accurate value for the nondimensional correction factor. Lastly, image processing techniques for comparing the porosity in the buffer between irradiation experiments were utilized as it resulted in the highest throughput for analyzing the characteristics of the fuel coatings. The results between these experiments are then to be examined and compared to find if there's any correlation between the porosity analysis results, the nanoindentation mapping, and the micro-cantilever beam testing. The data from these tests will be used to determine whether the buffer and IPyC coatings differ in their physical properties from AGR-1 to AGR-2. This work will inform future quality control efforts that will involve quickly probing buffer and IPyC properties to determine whether they are within an acceptable threshold.

3.2 Nanoindentation

3.2.1 Surrogate Particle Production

Early in the testing process, TRISO particles were required for the determination of suitable sample preparation methods for specimens and the

initial mechanical testing trials. However, since handling uranium-bearing material at ORNL includes oversight and safety procedures, surrogate-bearing TRISO particles were produced and used to develop the testing process. These surrogate particles utilized 400 μm diameter zirconia (ZrO_2) microspheres as the substitute for UO_2 or UCO found in fuel. Forty-gram charges of the ZrO_2 were already weighed, filtered through a roller micrometer to ensure particle sizes, and tabled to separate out any faceted or damaged microspheres in accordance with past AGR surrogate particle coating runs. These particles were then coated with the required TRISO layers under the same deposition conditions as AGR-1 variant 3 particles. Two of these coating runs were performed; the first with full TRISO coatings and the second excluding the OPyC. The second coating run was carried out due to information gathered during tensile specimen preparation. Images of particles from both batches can be seen in Figure 19.

3.2.2 Sample Polishing and Preparation

Initial sample polishing trials were performed on TRISO Surrogate Run 1 particles to determine which combination of polishing techniques resulted in the best polish for both the buffer and IPyC. The primary criterion for polish quality was the overall flatness across the buffer and IPyC. This was the concern as sudden height differences are likely to skew indentation results, which are likely to be found at the boundary where the polishing can affect the two coatings differently. Hexagonal patterns of 19 surrogate particles were mounted in thermoset epoxy for each irradiation experiment. The initial polishing steps followed the same methods established during the AGR program in utilizing a series of 9 and 6 μm polishing pads initially. Since the final two polishing pads used in the process appear to be the primary factor in the overall finish of the specimen, a testing matrix was created using a variety of 3 and 1 μm polishing pads. Three pads of each size were utilized in combination to produce a series of nine specimens for testing the overall polish quality.

3.2.3 Keyence Topography Mapping

To quantify the surface finish of the various polishing schemes tested, a Keyence VHX-6000 was adopted to map the surface of the polished TRISO surrogate cross-sections. Utilizing a method called Depth from Defocus, the software can recreate a 3D height map of a surface by taking a series of 2D images as the focus shifts in height. In each of the nine polishing trials, three height maps of the buffer and IPyC were produced. These examinations were only performed on the center particle in each mount at first, as it is believed to show the best polish. A point-to-point height line was then produced across the map of the two coatings to determine the maximum height difference for each trial. The results from the three tests on each particle were averaged to determine the polishing method that produced the flattest surface. The mount



Figure 19: Images of the surrogate TRISO particles used in sample preparation testing. TRISO Surrogate Run 1 is shown on the left and TRISO Surrogate Run 2 is on the right.

that demonstrated the best polish was then mapped on three separate particles to ensure the overall consistency of the polish. The results of this polish study are shown in Table 1.

AGR-1 baseline and variant experiments all consisted of several batches of coating runs being blended together to produce the fuel composite needed for each experiment. It was then decided that only particles from the first batch from each AGR-1 variant would be tested. Even though the batches for each respective irradiation experiment were run with the same coating conditions, it was thought best to avoid the potential for variances between batches during initial testing. This resulted in the production of four mounts in total: three being from the first batches of AGR-1 baseline and variant experiments and one being from the only batch of AGR-2 particles. The particles for each batch were also mounted in the same hexagonal pattern containing 19 particles. When it came to polishing the AGR-1 and AGR-2 particles, the best method determined during surrogate experimentation was utilized to polish the particles to approximately mid-plane. An identifying marked was then etched into the mount to signify the "northern" face of the mount to determine how the mount is oriented when placed into the nanoindenters and SEM. The particles are numbered 1-19 based on the scheme shown in Figure 20, so that nanoindentation data can be correlated with SEM imaging.

3.2.4 Indentation Methods

Nanoindentations were performed on an Agilent G200 Nanoindenter to carry out hardness and elastic modulus measurements across the buffer/IPyC boundary. Rectangular indentation schemes consisting of several indents were made spanning the buffer and IPyC so that the relation between the distance from the boundary and nanoindentation data can be found using an image analysis program. All indentations were originally performed with a nominally 60˚ cono-spherical tip with a 1 μm radius (SEM imaging from the factory shows the angle of the tip to be approximately 64˚ 25' and the radius to be 1018.74 nm). This tip was chosen for its circular indentation cross-section, as the standard berkovich tip and other various pyramidal indenters produce pointed polygonal indents. These types of indenters would likely produce scattered results near the buffer/IPyC boundary (where the mechanical properties shift abruptly) based on the indenter tip orientation. However, the tip was damaged when placed inside of an AFM for geometric calibration. A standard three-sided, diamond berkovich tip was utilized in its place as it was the only remaining tip on hand. While it may be expected to produce more scattered data, it will show trends between AGR-1 and AGR-2 coatings. Data was collected for AGR-1 particles using the conical tip in its uncalibrated state, so trends in the hardness plots between the two tips can be compared for AGR-1 particles.

Before any indentations are made, the tip is pressed into a dense, polished block of polystyrene to both clean the tip (Fischer-Cripps 2011) and

Table 1: The results from mapping the surface of 9 particles each polished using different combinations of polishing pads.

Keyence Mapping Results					
Test #	ΔHeight #1 (mm)	ΔHeight #2 (mm)	ΔHeight #3 (mm)	Avg.	Stdev.
1	0.654	0.680	0.344	0.559	0.187
2	0.629	0.922	0.254	0.602	0.335
3	0.335	0.383	0.384	0.367	0.028
4	0.407	0.202	0.318	0.309	0.103
5	0.684	1.056	0.681	0.807	0.216
6	0.159	0.594	0.353	0.369	0.218
7	0.148	0.205	0.243	0.199	0.048
8	0.334	0.348	0.714	0.465	0.215
9	0.385	0.148	0.343	0.292	0.126

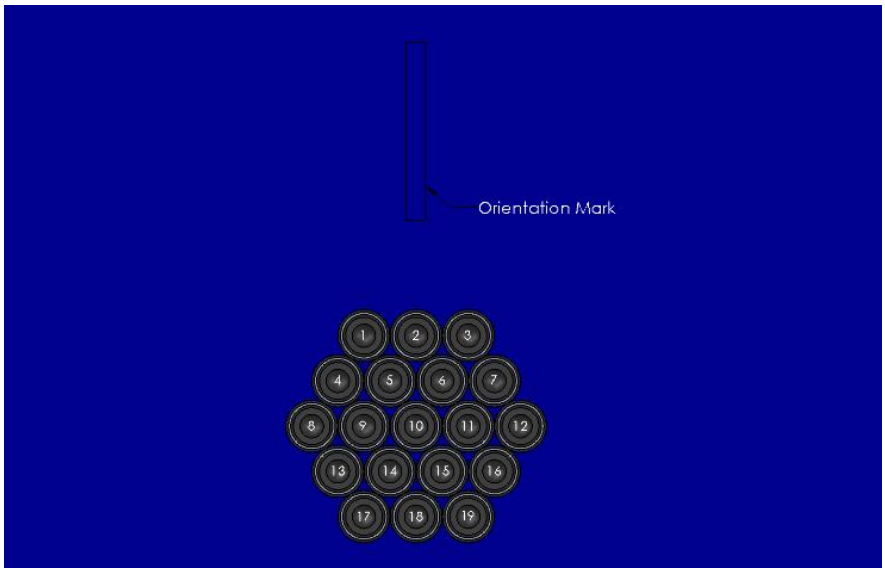


Figure 20: Shows the particle designation for particles mounted into a hexagonal pattern for use in identifying the locations of indentation schemes.

align the indentation location to the microscope positioning mark. A series of 140 indentations are made in a 10x14 array in CSM mode under a constant loading rate of 500 μN/s. Indentations were performed to a depth of 1000 nm and measurements for the mechanical properties are averaged over a depth of 500 to 900 nm since the tip calibration was performed over this range. This target depth was chosen as a compromise between testing the largest volume possible and decreasing the spacing between each indent in an act to increase the resolution of the indentation map. The recommendation for spacing nanoindentations is that the distance between indents should be at least between 3-5 times the diameter of the residual impression from the indent (Fischer-Cripps 2011). However, after initial testing it was found that the berkovich would not leave an easily discernable indent into the coatings, so a spacing of approximately 1.5 times the diameter at maximum indentation depth was chosen to increase the mapping resolution, resulting in indentations being spaced 13 microns apart from one another. The Poisson's ratio for both the buffer and IPyC were taken to be 0.23 as used in TRISO particle models (L. Knudson, K Miller et al. 2009). The Poisson's ratio and elastic modulus for the diamond tip were set to the default values in the tip calibration program of 0.07 and 1,141 GPa.

3.2.5 Nanoindenter Tip Calibration

Calibration of the berkovich tip's projected area function coefficients were performed based on the instructions given in the Agilent G200 user manual. This process entails making indentations into a smooth fused silica sample provided with the nanoindenter. Fused silica has a known elastic modulus of 72 GPa, making it an ideal material for tip calibration. An array of 25 indentations were created on the sample to a depth of 1000 nm. The load and displacement data are then extracted for each indent. Using this information, a program within the indentation software will calculate the necessary area function coefficients for the elastic modulus calculated for the 25 indents to match the 72 GPa of the fused silica as best as possible over some range in the indentation depth. For the purposes of this experiment, the area function for the tip was fit over the 500-900 nm depth range and the area function was determined up to the default two coefficients.

3.2.6 Data Analysis

Once indentations were performed on a sample, a method was needed for determining each individual indentation's distance from the buffer/IPyC boundary. Therefore, a Matlab program was written that utilizes SEM images of the indentation scheme to do just this. Images of the indentations were taken with a Phenom XL SEM. These images were then run through a Matlab script that allows you to mark the center of indentations located at the boundaries of the indentation scheme. These boundaries are based off of the indents performed in

the SiC coating as the indents into the buffer and IPyC are primarily elastic and don't leave behind a discernable indentation mark. These locations along with the distances between indentations and the total number of rows and columns produced then grant the program enough information to extrapolate the center points of each indentation data point. Next, the location of the buffer/IPyC boundary must be deciphered by the program. This is accomplished by allowing the user to click on points along the coating boundary. The program then uses image features such as contrast and brightness to trace a line along the boundary connecting the user-inputted points. The result of one of these indentation maps appears in Figure 21.

The Matlab code then determines the distance from each indentation point to the nearest point on the boundary line in terms of pixels. This value is essentially the tangential distance of the indent to the apparent boundary between the buffer and IPyC. An Excel sheet is then output that numbers the indentations based on the same raster scanning method that the nanoindenter utilizes, along with each point's distance to the boundary line. The distance values are then converted from pixels to microns by using the software ImageJ to determine the conversion factor based on measuring the scale bar output by the SEM in pixels. Finally, the hardness and elastic modulus values found using nanoindentation can be transferred to the Excel chart so that the two values can be mapped as a function of distance from the boundary. From here, plots and comparisons can be made between the characteristics of different fuel variant coatings from AGR-1 and AGR-2.

3.3 Tensile Testing

3.3.1 Spherical Coating Specimen Preparation

To produce tensile specimens composing of the buffer/IPyC bond, the coatings must constitute the entire cross-section of the gauge length of a specimen at some point. This would result in an exceedingly miniscule cross section for a tensile specimen on the order of just hundreds of microns thick. The buffer/IPyC bond would also have to have the weakest point in the sample to ensure that the ultimate tensile strength being measured is that of the buffer/IPyC boundary region. This complication appeared early in the development of the tensile specimen fabrication process, as it was noted that the OPyC would readily delaminate from the SiC. This is the reasoning for why TRISO Surrogate Run 2 was produced under the same conditions as the first run but excluded the deposition of the OPyC coating to circumvent the weak bonding to the SiC during tensile testing. Once the tensile testing would have been expanded to the examination of AGR fuel coatings, the OPyC would have been oxidized in a furnace to burn back the coating to the SiC to recreate the surrogate coating

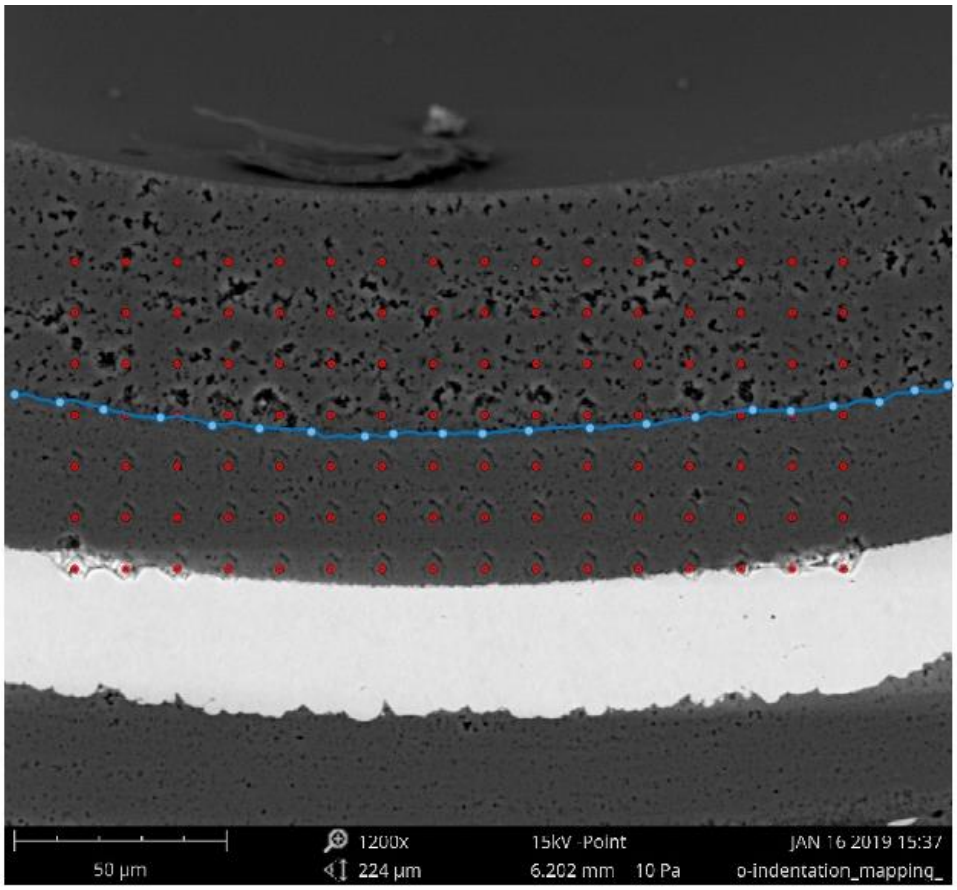


Figure 21: A map of nanoindentation locations and the buffer/IPyC boundary across a surrogate TRISO particle's cross-section produced by way of a Matlab program. Where the red points indicate the indentation locations and the blue line denotes the buffer/IPyC boundary.

conditions. The geometry of an “ideal” tensile specimen of this scale containing TRISO coatings is shown in Figure 22.

The fabrication of specimens for tensile testing of the coating boundary was attempted based on the SS-Mini tensile specimen geometry. TRISO Surrogate Run 2 particles were mounted in a clear epoxy and polished to half plane. The kernels were dropped out and epoxy was set over the exposed half particles. These epoxy-encased coatings were then cut into slabs, each containing a single particle. The slabs were then polished down on two sides to expose the coatings within the epoxy. An illustration of the fabrication process for these slabs is shown in Figure 23.

To create the dog bone shape necessary for tensile testing, two machining methods were attempted. First a wire-cut electrical discharge machine (EDM) was utilized to cut through both the epoxy and particle. This equipment was chosen for its non-contact method for material removal and was therefore well-suited to machine such a delicate specimen, where the gauge section would measure only a few hundred microns wide. However, the SiC was unable to effectively conduct the current required to erode it. Therefore, methods for fabrication transitioned over to more conventional end mill cutting techniques. The usage of an end mill allowed for the machining of a tensile specimen with gauge dimensions of approximately 390 μm thick and 240 μm wide. Only one specimen was produced using this process. The resulting tensile specimen is found in Figure 24.

3.3.2 Flat Coating Specimen Preparation

While the development of the methods used to fabricate a dog bone specimen were ongoing, a process was developed to determine whether the buffer/IPyC bonding region is the weakest part of the surrogate fuel coatings. Therefore, three 0.375 inch diameter by 0.020 inch thick sapphire disks were added to the fluidized bed during the chemical vapor deposition of TRISO Surrogate Run 2 particles. This would allow for the production of flat coating specimens as the coatings don’t fully bond to the sapphire and can be easily cut free of it. These flat specimens are larger than the spherical fuel coating and avoid any discrepancies related to the curved geometry of the coatings. These features significantly simplify the process of producing tensile specimens. One tensile specimen was produced using this flat coating geometry. The sample was produced using a method similar to the mounting and polishing steps used for creating the dog bone geometry specimen. However, this sample was polished to produce a specimen with a square cross-section 2mm wide. An image of the specimen that was produced using this method is shown in Figure 25.

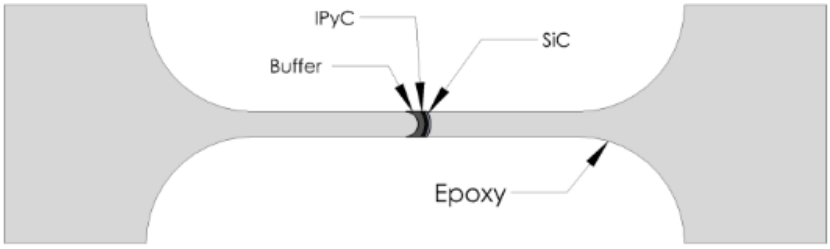


Figure 22: A model of a tensile specimen with the “ideal” geometry for testing the tensile strength of the buffer.

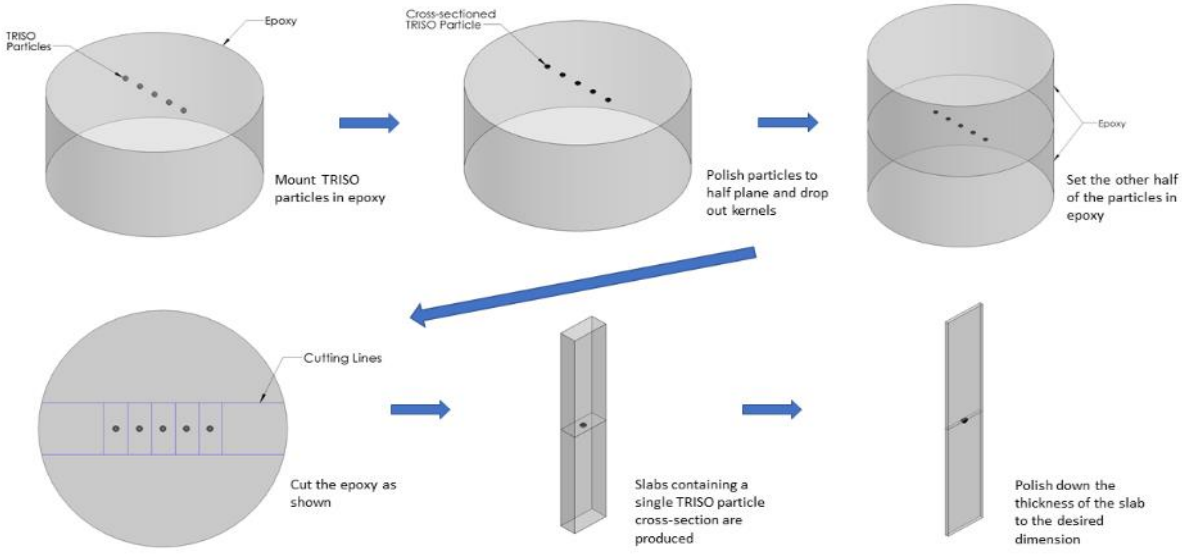


Figure 23: The sample preparation method for producing slabs of epoxy encased TRISO particles for use in tensile testing experiments.

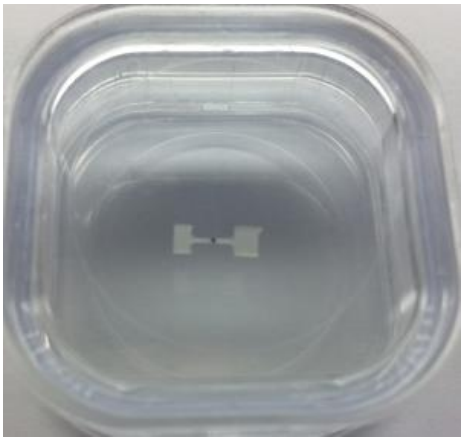


Figure 24: The sole dog bone specimen produced for tensile testing of the buffer/IPyC boundary.

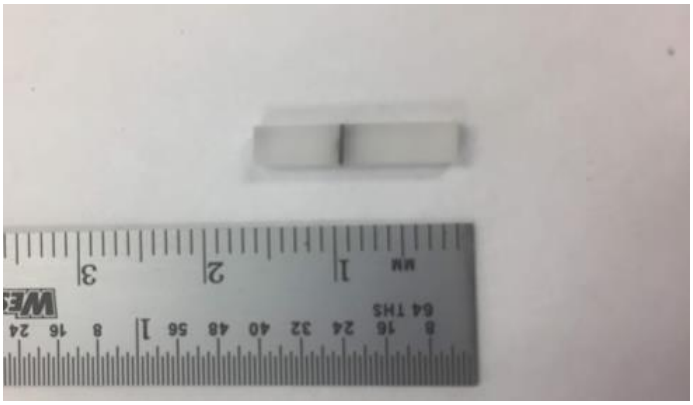


Figure 25: An image of the tensile specimen produced to determine the weakest coating bond in the TRISO fuel form. The flat coating specimen is wedged between two clear epoxy arms.

3.3.3 Tensile Testing

Testing the strength of the coatings in the flat coating specimen required a method to grasp it, so a binding barrel was placed over each end of the gauge length and glued into place to act as heads for the tensile frame to grip. An alignment tool was 3D printed to guarantee that the specimen is aligned within the binding barrel. The sample was then loaded into an MTS Insight tensile frame as shown in Figure 26 and loaded under uniaxial tension until fracture occurred. In this initial experiment the IPyC/SiC interface fractured instead of the buffer/IPyC boundary. It was speculated that this may have been the result of the mechanical polishing damaging the SiC, introducing stress concentrations at the IPyC/SiC interface. This result contributed to the decision to move to another form of mechanical testing for use in coating characterization.

3.4 Cantilever Beam Testing

3.4.1 Sample Preparation

Micro-cantilever beam specimens were produced by first mounting and polishing particles to half-plane using the same methods outlined in the preparation of nanoindentation samples. Only two mounts consisting of AGR-1 variant 3 and AGR-2 particles were polished for this purpose as the time required to produce cantilever specimens limited the total number of test cases. The mounted particles were then carbon-coated to reduce charging in the SEM. Cantilever beams with a pentagonal cross-section were produced by way of FIB milling. This was achieved by milling vertically on either side of the beam location, and then tilting the SEM stage to undercut the beam from either side at a 45-degree angle. One end of the resulting beam was then milled off to have only one fixed end. An FEI Quanta 3D 200i Dual Beam instrument was used to produce the rough cuts for the trenches around the cantilever beam using a beam current of 30 to 50nA. This was the highest milling rate available while avoiding drifting of the image. However, it was discovered that using a beam current of this magnitude resulted in indirect damage to the cantilever beam. Therefore, platinum was deposited beforehand across the top surface of the specimen where the cantilever beam would be located to prevent deterioration to it. Redeposition of the carbon, however, proved to be a matter of concern, forcing repeated passes with the FIB. Finer milling cuts were then made with an FEI Versa 3D Dual Beam instrument using a beam current of 3 to 7nA to clean up the edges of the sample. The platinum coating covering the top of the specimen would typically remain atop the beam as milling it away could result in damage to the beam. This milling resulted in a beam spanning the buffer and IPyC coatings, where the base of the beam was located inside the buffer and the beam would be loaded at some point within the IPyC. The bases of these beams were placed at various depths in the buffer from the buffer/IPyC boundary. This would allow

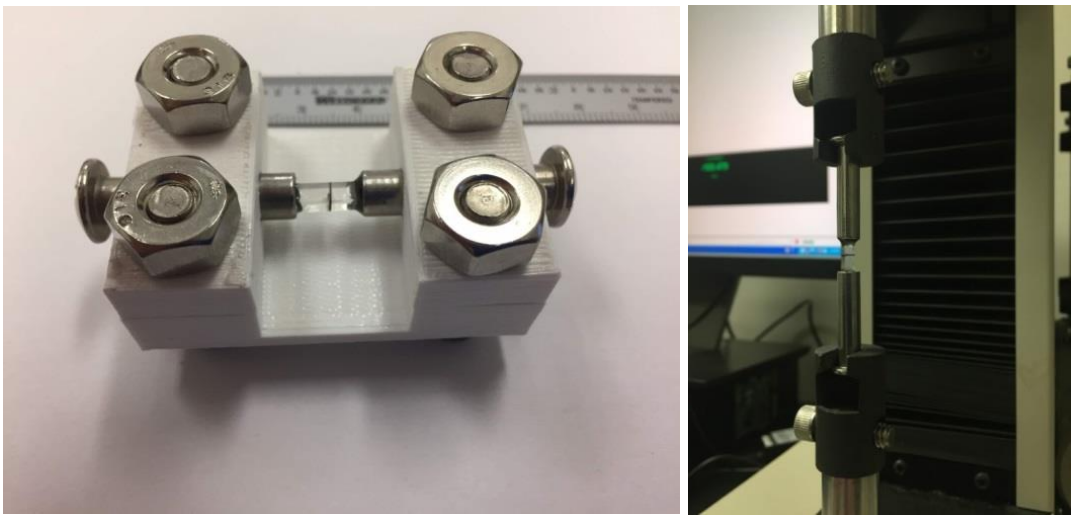


Figure 26: (Left) An image of the tensile specimen within its mounting apparatus and 3D-printed alignment tool to the left. (Right) The tensile specimen is loaded into an MTS Insight tensile frame on the right.

for several points of comparison between AGR-1 and AGR-2 particles. This would also allow for the measurement of mechanical property changes as a function of distance from the boundary. An image of one of the resulting specimens is shown in Figure 27. The final dimensions for the cantilever beams measured approximately 25µm long by 10µm wide with 7µm flats on both sides.

3.4.2 Beam Loading

Cantilever specimens were imaged and loaded inside a Tescan Mira3 SEM with an in-situ nanoindentation frame. A flat, diamond tip with a 10µm diameter was utilized for loading each specimen. The nanoindenter tip is placed at the end of the cantilever beams for loading, where the corners of the beam are coincident with the circumference of the nanoindenter tip. An image depicting the placement of the tip is shown in Figure 28. Placement of the tip at the end of the micro-cantilever beam was performed by incrementally moving the tip closer towards the surface of the material until a shadow appears directly below the tip. This shadow is then placed directly over the end of the beam similarly to that shown in Figure 28. The surface of the material is then found by forcing the tip to contact the IPyC or buffer several microns away from the cantilever beam and surrounding trench. This allows the tip to make a quick approach before the displacement-controlled loading begins. The displacement rate for the tests was set to 50nm/s up to a maximum depth of 10,000nm until fracture occurred within the beam and load and displacement values were tracked during testing similarly to the standard nanoindentation tests. Images were taken of the beam both before and after testing and video was taken over the course of loading.

Flexural stress of the beams will then be calculated for the top of beam at the location of fracture where the surface is in tension, however, due to the pentagonal geometry of the beam cross-section, the bottom of the beam experiences the highest stresses. Since graphite generally has a higher compressive strength than tensile strength, these beams should fracture under tension starting at the top surface. Further study however would be required to prove whether compressive failure is occurring during the loading of these beams. Calculating the flexural stress will be calculated using the following equation.

Equation 8: $$\sigma_{FS} = \frac{FLc}{I}$$

This equation gives you the flexural stress at any point in a beam assuming it is loaded as a point load at the end of the beam. While this is not the exact case, this will be assumed as the ever-changing contact of the nanoindenter tip with the beam during testing complicates calculations. In this equation F is the load on the beam at fracture. The value L is the distance from the point load (or the end of the beam) to the location of fracture. Then c is calculated as the distance from the center of mass of the beam cross-section to

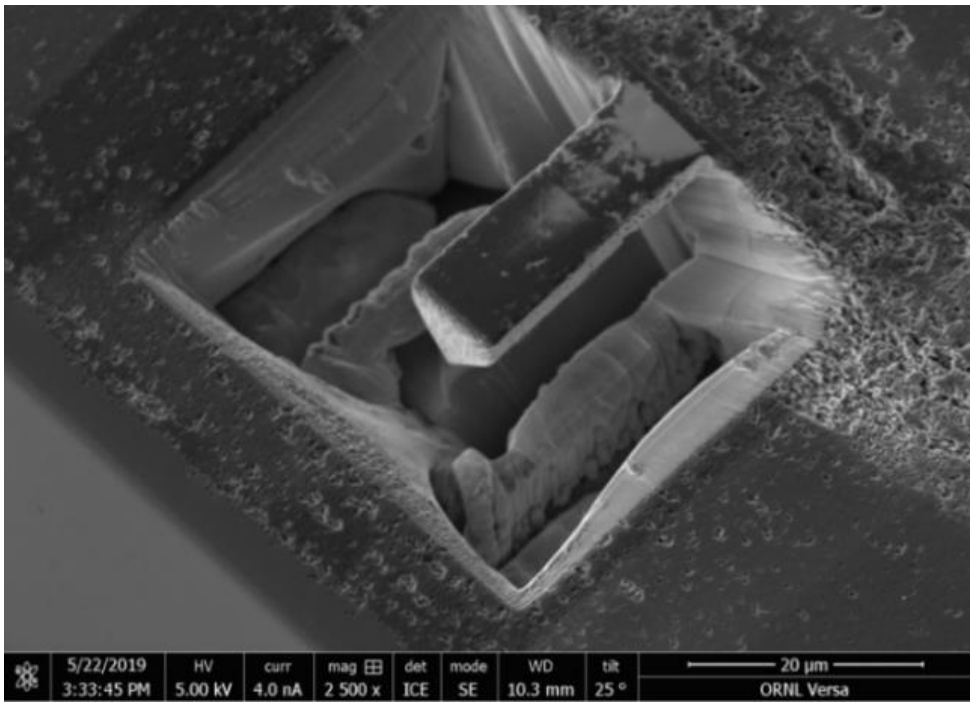


Figure 27: An image of a FIB-produced micro-cantilever beam spanning the buffer and IPyC of a TRISO particle cross-section. The buffer is the porous medium in the top right corner of the image, while the IPyC is the relatively smoother portion throughout the center of the image adjacent to the buffer.

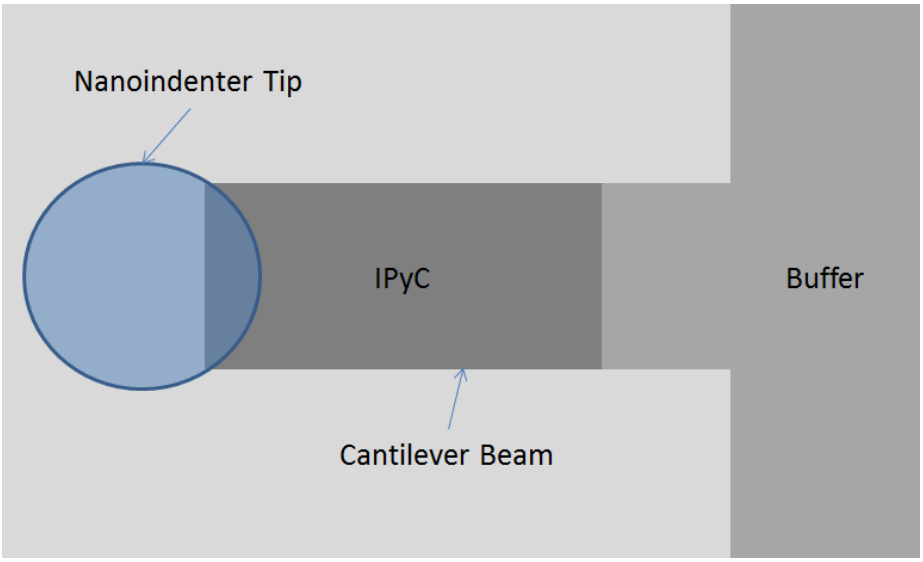


Figure 28: The illustration shown above depicts the nanoindenter tip placement when loading the micro-cantilever beams.

the extreme fibers of the beam (top of the beam). Lastly, I is the second moment of area for the beam cross-section. It will be assumed that all of the micro-cantilever beams will have the same dimensions in these calculations. While these beams are porous (which would result in complex stress concentrations throughout the beam) due to the nature of the buffer and IPyC, they will be treated as homogeneous for use in this equation as this is a comparative study and aren't concerned with investigating the intrinsic mechanical properties of the pyrolytic carbon.

3.5 Image Processing of Porosity

To allow for the measurement of porosity found in the buffer, the mounts used in the nanoindentation process were also used for porosity imaging purposes. A Leica DMRX was then utilized to image a portion of the buffer, IPyC, and SiC for each particle on the mount. For the brightness between images to remain somewhat consistent, the lighting was adjusted so that the bottom right-hand region of the SiC read an 8-bit greyscale value between 240 to 250 for every particle, meaning that the SiC appeared around the upper threshold of the brightness value. These images were then processed using ImageJ to determine which pixels corresponded to pores. This was performed by thresholding the image to 115, meaning any pixel equal to or below the 8-bit greyscale value of 115 is set to black, while the remainder of the pixels are set to white as shown in Figure 29. A Matlab program was then created that would determine the porosity of the buffer as a function of the distance from the buffer/IPyC boundary. This program works by allowing the user to place three points along an image of the boundary and overlaying an arc that fits those three points as shown in Figure 29. The porosity as a function of distance from the boundary is then calculated by a function that finds the shortest distance of each pixel within the buffer to the nearest point on the user-generated arc. Portions of the buffer in these images are effectively edited out as the actual nearest point to the boundary from these pixels are outside of the bounds of the image. The distances calculated for each pixel are then converted from pixel values into microns based on a scaling factor previously determined for the Leica with the 50x objective and 1.25x zoom used in this process. Distances from the boundary for both porous and non-porous pixels are then compiled into 1 μm bands up to 60 μm into the buffer. The percentage of porosity within each 1 μm increment is the found by calculating the ratio of porous pixels to the total number of pixels within each band. These values are then exported into an excel chart and bar graphs are produced for each image displaying how the porosity evolves within the buffer as a function of its distance from the buffer/IPyC boundary.

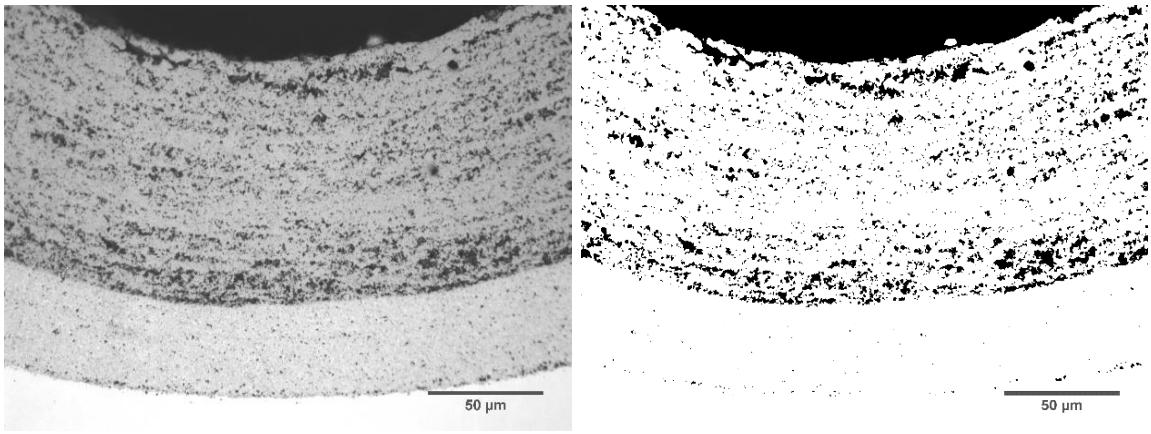


Figure 29: (Left) A cross-section of a TRISO particle's buffer, IPyC, and SiC with a black line defining the buffer/IPyC boundary can be found on the left. (Right) A black and white threshold image of the same particle.

CHAPTER FOUR
RESULTS AND DISCUSSION

Three different testing methods were applied to characterize AGR-1 and AGR-2 buffer and IPyC coatings, with each set of particles comprised of only one batch of particles from each irradiation experiment. Nanoindentation arrays were performed on particles from AGR-1 baseline, AGR-1 variant 1, and AGR-2 particles. Micro-cantilever tests were performed on AGR-1 variant 3 and AGR-2 particles. Porosity analysis was performed on AGR-1 baseline, AGR-1 variant 1, AGR-1 variant 3, and AGR-2 particles. Efforts to perform nanoindentation tests on AGR-1 variant 3 particles are currently underway.

4.1 Nanoindentation

A total of thirty-two particles were characterized using nanoindentation testing. Nine of these particles were from the AGR-1 baseline experiment, seven were from AGR-1 variant 1, and sixteen came from AGR-2. Particles from AGR-1 variant 3 were not tested as the mount prepared for this purpose was contaminated during preparation of another specimen and relegated to micro-cantilever testing. No other AGR-1 variant 3 particles were readily on-hand to produce another mount. A graph displaying the indentation results of three particles from AGR-1 variant 1 are found in Figure 30. In this plot, negative values denote the distance from a given indent within the buffer to the IPyC/buffer boundary, while positive values represent the distances of indents within the IPyC from the same boundary. Each point on the graph represents the hardness value found for a single indent and each color represents the results from a distinct particle.

As can be expected, the hardness takes a sharp decline from the IPyC into the buffer. Average hardness values for both the buffer and IPyC were calculated to identify any obvious coating property differences. These averages and their standard deviations can be found in Table 2. The values found for the hardness are either below or on the low end of values found in a past study where acetylene-derived pyrocarbon (buffer) measured anywhere from 4.8 to 1.5 GPa and 4.0 to 2.9 GPa for acetylene/propylene-derived pyrocarbon (IPyC) (López-Honorato, Meadows et al. 2008). Coatings in that study, however, were coated onto an alumina substrate and inside of a smaller coating chamber with multiple gas inlets, all of which could have affected coating properties.

Both AGR-1 baseline and variant 1 particles showed nearly identical average hardness values for both the IPyC and buffer, with the baseline particles giving 1.02 GPa for the buffer and 3.23 GPa for the IPyC while variant 1 particles

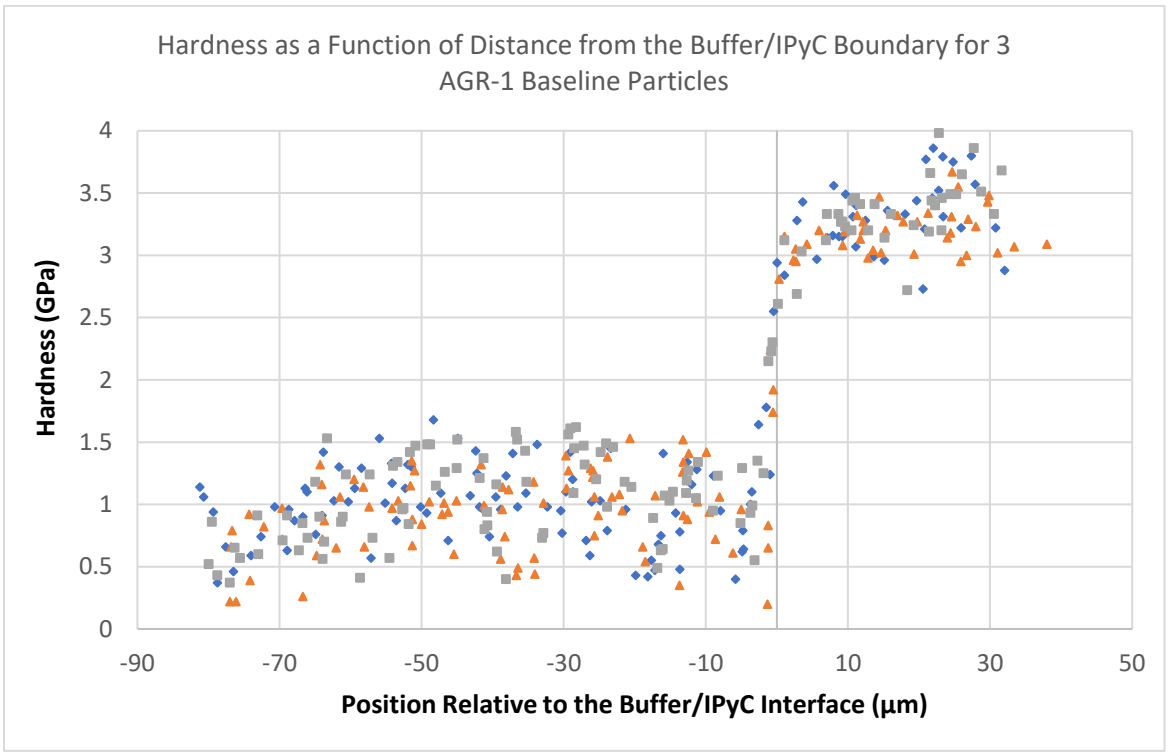


Figure 30: Shows plots displaying the change in hardness in relation to distance from the buffer/IPyC boundary for three particles. Negative values denote distances within the buffer. Each color corresponds to the results from a different particle.

Table 2: Shows the results of taking the average hardness for the IPyC and buffer for AGR-1 baseline/variant 1 and AGR-2

	AGR-1 Base	AGR-1 V1	AGR-2
Average Buffer Hardness (GPa)	1.02	1.03	0.80
Buffer Hardness Stdev (GPa)	0.06	0.03	0.07
Average IPyC Hardness (GPa)	3.23	3.26	2.87
IPyC Hardness Stdev (GPa)	0.06	0.08	0.07

gave a hardness of 1.03 GPa for the buffer and 3.26 GPa for the IPyC. The results from AGR-2 indentation testing however result in an average hardness of 0.80 GPa for the buffer and 2.87 GPa for the IPyC. This disparity in hardness between the two irradiation experiments may be the result of an increase in porosity for AGR-2 buffer coatings as more porosity results in less volume to resist the deformation cause by indentation, leading to a lower hardness value. An increase in porosity could also correspond to higher stresses in the buffer since there is less material to distribute forces across and more stress concentrations in the coating. This is relevant as higher stresses would occur as the buffer densifies and pulls away from the IPyC, causing the buffer to tear with less force for more porous materials. Therefore, the reduced hardness found in the buffer of AGR-2 particles compared to that of AGR-1 particles could likely correspond to a lower effective tensile strength if this discrepancy in the hardness is due to a variation in porosity. This could help explain why fractures propagating into the IPyC have been found to be much more prevalent in AGR-1 particles during irradiation testing as the buffer itself would be notably stronger than its AGR-2 counterpart.

While the overall characteristics of the buffer are useful for gleaning information, the region of the buffer directly adjacent to the IPyC is of the most interest as that is where tearing often occurs during irradiation testing. Therefore, analyzing the indentation data adjacent to the buffer/IPyC boundary could prove highly beneficial. Looking over the indentation plots however shows that a relatively high scatter exists in the data as seen with all arrays in Figure 30. Therefore, low pass filters must be placed on the data for it to show any trends that may arise in the hardness of the buffer as a function of distance from the boundary. To smooth out the data in this manner, a moving average was taken of the hardness and position values. This moving average included a central data point averaged along with a single data point preceding it and a single point following it. Three data points were chosen for the moving average calculations as choosing more points might result in hardness values in the area of interest near the boundary to be misrepresented due the existence of the much harder IPyC in proximity. A plot showing the effect of this filtering can be seen in Figure 31. This smoothing of the data was performed on the data from all thirty-two indentation arrays. This allowed for a more straightforward analysis on the general trends of mechanical properties within the buffer.

Looking at the hardness plots produced by this filtering method, it can be challenging to find any consistent trends in the hardness data within the buffer as the peaks and valleys seem to fluctuate randomly in value and location. The values of hardness in the buffer also occupy a wide range of value reaching values of just over 1.5 GPa down to 0.5 GPa and below. One noticeable trend however is that in many cases the hardness within the buffer takes a rather sizeable drop in value relative to the rest of the buffer within the first 20 or so microns. This dip in hardness values results in an easily discernable local and in many cases absolute minimum hardness value. With this information we can

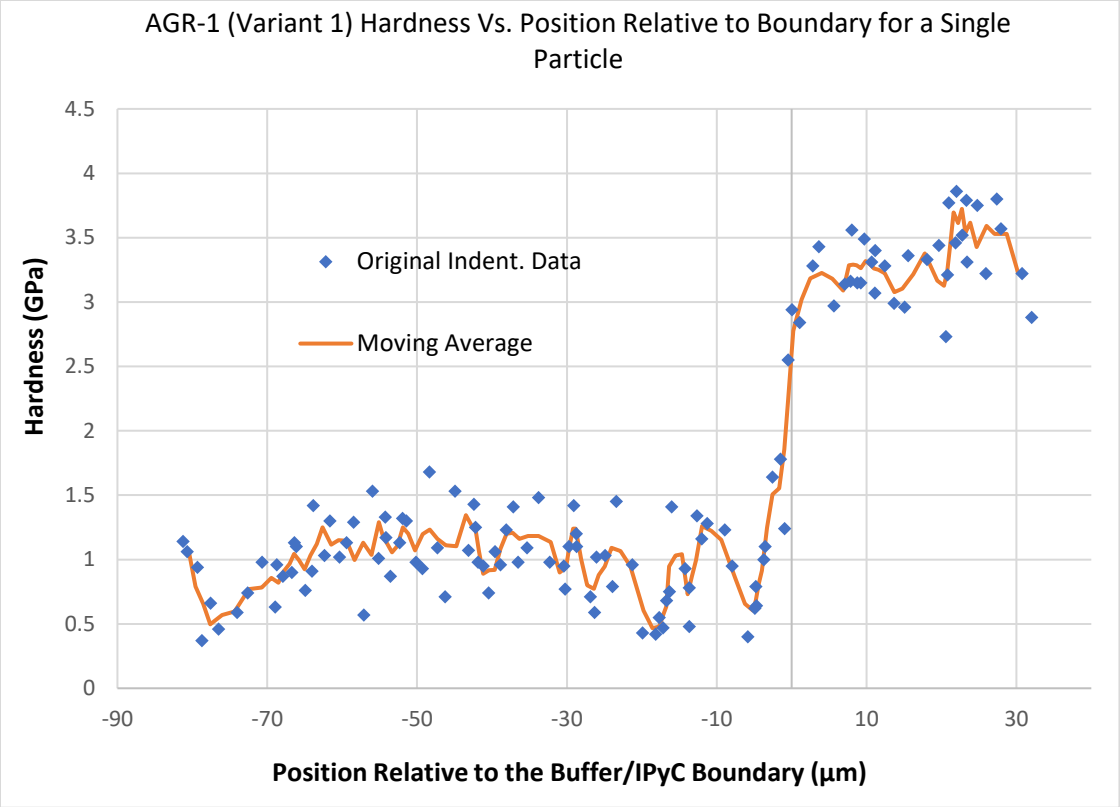


Figure 31: A plot showing the effective filtering achieved by taking the moving average of the hardness as a function of distance from the boundary, where negative values represent points in the buffer and positive points are for indents made inside the IPyC.

extract this minimum hardness value within the first twenty microns of the buffer adjacent to the boundary for each indentation series to compare between irradiation experiments. Only minimums from the moving average data set will be considered as the relatively high level of scatter from the raw data set doesn't allow for a clear picture of characteristic hardness at a given distance from the boundary. Shown in Table 3 are the results of extracting this minimum hardness value as well as where in the 20 μm adjacent to the boundary these values are found within the moving average data set. Hardness values highlighted in blue are also the absolute minimum value throughout the entire data set for each particle. From this it can be determined that for the thirty-two particles tested, over half of them had their three adjacent points of lowest hardness on average within 20 μm of the boundary. This finding falls in line with PIE results often showing tearing in the buffer bordering the boundary as a region of weaker mechanical properties would result in a preferred path for crack propagation. When comparing the actual hardness values between irradiation experiments, we find that the minimum hardness values in the AGR-1 baseline experiment average at around 0.57 GPa, while AGR-1 variant 1 particles average 0.48 GPa, and AGR-2 particles come out as the lowest at 0.37 GPa. These values again support the theory that AGR-2 particle coatings differ in strength to AGR-1 particle coatings and may result in a more favorable tear behavior within the buffer.

While nanoindentation testing with the berkovich tip has allowed for the deduction of invaluable data, it is worth comparing to the results found using a conical tip originally chosen for characterizing these particle coatings. As mentioned in section 3.2.4, a conical tip was originally chosen for its circular indentation cross-section which may have resulted in a more accurate measure of hardness near the buffer/IPyC boundary. However, this tip was damaged during calibration of the tip's geometry, but not before nine indentation series were performed on various AGR-1 particles similarly to how tests were performed with the berkovich tip. No indentation data with the conical tip exists for AGR-2, making comparisons with that tip between AGR-1 and AGR-2 particles impossible. Nevertheless, the results for both tips on AGR-1 particles can be studied to discern any discrepancies that may occur. Shown in Figure 32 are two indentation plots like ones shown earlier. One set of points are for conical tip indentations while the other displays the results found using the berkovich tip. Both indentation sets are from separate AGR-1 variant 1 particles but are fairly characteristic of other indentation plots produced by their respective tips. The data clearly shows that the indentations performed utilizing a conical tip reduce scatter and results in a more well-defined hardness curve across the coatings. While outliers still exist in the conical tip data, the general trends in the changing hardness values are much more evident than in the berkovich tip data set. One reason for this inconsistency between the data likely relates to the depths at which both tips were tested. To avoid overlapping of the indents, tests with the berkovich tip were only taken to a depth of 1000nm averaging the hardness from

Table 3: The table below shows the minimum hardness values found in the 20 microns of the buffer adjacent to the buffer/IPyC boundary for individual particles. Values in blue are also the absolute minimum hardness values found throughout the buffer.

	AGR-1 Baseline		AGR-1 Variant 1		AGR-2	
	Min Hardness (GPa)	Location (µm)	Min Hardness (GPa)	Location (µm)	Min Hardness (GPa)	Location (µm)
	0.47	18.6	0.37	4.1	0.44	9.8
	0.56	1.3	0.49	5.4	0.39	12.6
	0.59	16.4	0.48	10.0	0.23	9.6
	0.79	14.3	0.39	6.5	0.42	5.4
	0.40	4.3	0.60	13.8	0.30	18.7
	0.61	8.7	0.62	4.0	0.50	7.1
	0.53	6.7	0.46	5.3	0.43	6.7
	0.38	8.5			0.28	12.2
	0.83	17.7			0.33	11.8
					0.41	8.4
					0.31	4.6
					0.58	18.9
					0.31	16.7
					0.58	10.2
					0.25	7.6
					0.22	5.7
Mean:	0.57	10.7	0.49	7.0	0.37	10.4
Stdev:	0.15	5.9	0.09	3.3	0.11	4.4

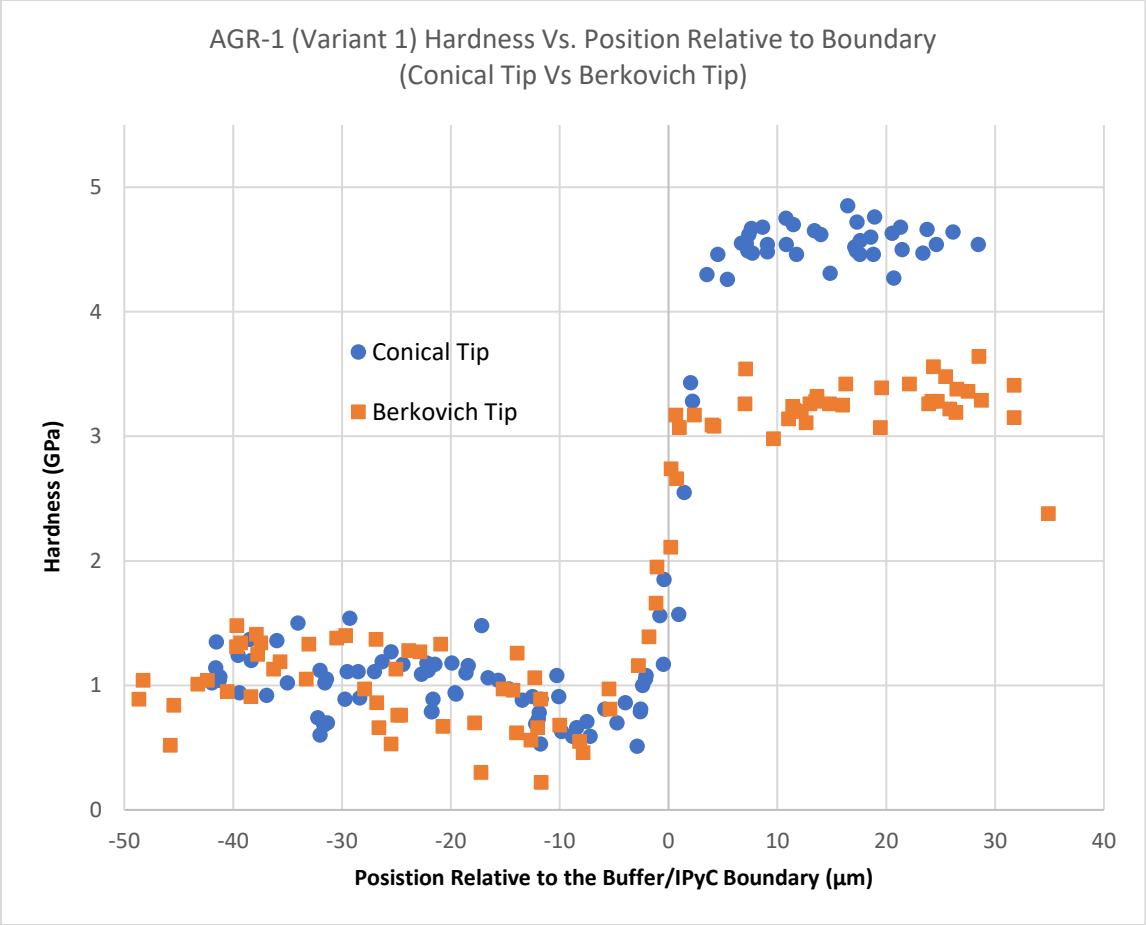


Figure 32: A plot demonstrating the differences between the nanoindentation results found using a berkovich and a conical tip.

500-900nm while the conical tip used formed a 60° cone and was therefore much less broad than the berkovich tip. This allowed for much deeper indents than the berkovich tip allowed for testing. Indents with the conical tip were taken to 2600nm in depth and averaged the hardness reading between 2000-2500nm. Measuring the theoretical volume of this indent using ideal geometry gives us around 14μm^3 for the conical tip and 6μm^3 for the berkovich tip at the maximum depth values used in averaging the hardness. This notable difference in the total volume tested could have resulted in the disparity in scatter found between the two data sets. Another point to consider is that the pointed geometry of a berkovich tip cross-section could have affected measurements near the buffer/IPyC boundary as mentioned in section 3.2.4. The points of this triangular cross-section protrude from the axis of indentation motion by twice as much as the center of each side of the triangular cross-section. Therefore, indents within the buffer near the buffer/IPyC boundary may or may not make contact with the IPyC depending on the orientation of the berkovich tip. This would presumably skew results found within a few microns of the boundary. The hardness values found within the IPyC between both data sets also diverge quite drastically based on this graph, but this may be due to the lack of accurate calibration testing for the conical tip.

4.2 Micro-Cantilever Beam Testing

In total, twelve micro-cantilever specimens had been produced and tested using the methods discussed earlier. Nine of these specimens had been made using AGR-1 variant 3 particles and the remaining three were milled from AGR-2 coatings. These beams were labelled A through I for the AGR-1 particles and A through E for AGR-2 particles (two of these beams were damaged during sample preparation, hence five beams instead of three). Fractures within the beams were originally expected to occur directly adjacent to the base of the beam in most cases as that is where the maximum stress would be located. However, many of these beams broke closer to the end of the beam while some even fractured past the base as shown in Figure 33. This was most likely the result of weaker regions in the buffer experiencing higher stresses due to the porous and heterogeneous nature of the buffer's properties already seen in the nanoindentation data. Data on where each beam fractured, the maximum load reached during testing, and the flexural strength of each specimen at the fracture location is tabulated in Table 4. All of these values were calculated as if the platinum coating on the top was a negligible thickness in relation to the thickness of the beam. Flexural stress values for cantilevers G and H from AGR-1 variant 3 were unable to be calculated due to notches being milled near the bases of each beam to test whether notched specimens would work well in forcing fractures at a specified location. These notches succeeded in this manner; however, they act as stress concentrators for the beam making any stress calculations more difficult and they

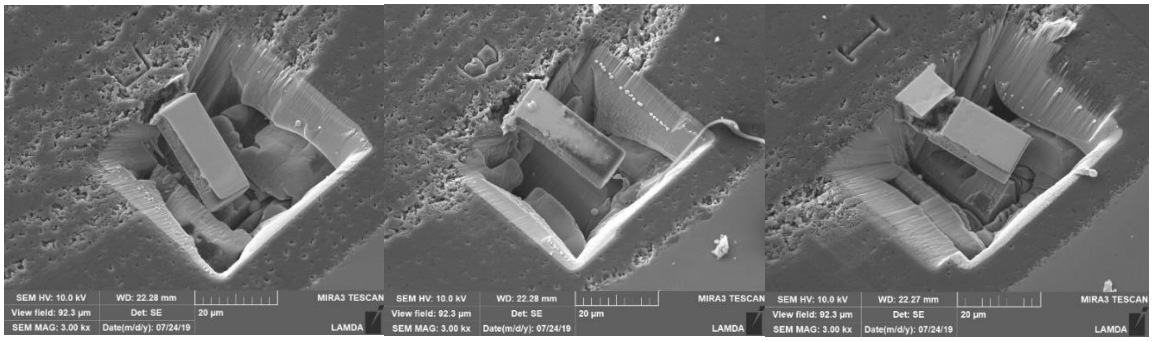


Figure 33: The images displayed above show the varying fracture characteristics of three separate micro-cantilever beams. All cantilevers come from AGR-1 variant 1 particles. (Left) Shows a beam that fractured at the base. (Middle) Shows one that has fractured beyond the base. (Right) Shows one that has fractured away from the base.

Table 4: The table below lists the results for all of the cantilever beams tested per irradiation experiment. Distances for where the beams fractured in relation to the boundary were estimated based on SEM images and corrected for the angle at which the image was taken.

AGR-1 Variant 3			
	Corrected Fracture to Boundary Dist. (µm)	Max Load (mN)	Flexural Stress at Fracture (MPa)
Cantilever A	21.0	2.020	302
Cantilever B	Fract. Beyond Base	1.595	239
Cantilever C	21.9	2.307	345
Cantilever D	27.6	1.385	207
Cantilever E	16.5	2.586	268
Cantilever F	13.7	2.936	351
Cantilever G	Notched	0.592	N/A
Cantilever H	Notched	0.129	N/A
Cantilever I	12.5	2.827	312
AGR-2			
	Corrected Fracture to Boundary Dist. (µm)	Max Load (mN)	Flexural Stress at Fracture (MPa)
Cantilever A	6.5	1.200	81
Cantilever B	Fract. Beyond Base	1.024	153
Cantilever C	9.4	Sample prep - Fract.	N/A
Cantilever D	10.2	Sample prep - Fract.	N/A
Cantilever E	18.5	1.228	184

require analysis of the fracture surface and modelling for any use in calculating the fracture toughness. Cantilevers C and D from AGR-2 also don't include any stress data as they fractured while preparing the mount for in-situ cantilever testing. Besides the aforementioned cantilevers, the only other variable between specimens was the distance from the base of each beam to the buffer/IPyC boundary.

Seeing as the cantilevers tore in varying locations, comparing data from both irradiation experiments becomes challenging. An accurate measure of the flexural stress does not exist for the cantilevers that fractured beyond their base, but the value displayed for it is at the least a stress that the base of the beam was able to withstand. Removing these beams and the notched specimens from the data set leaves six specimens from AGR-1 variant 3 and two from AGR-2 to contrast. Looking at just the flexural strength between the two it is easy to recognize that AGR-2 coatings average a lower strength of approximately 133 MPa versus an average of 298 MPa for that of AGR-1 variant 3 particles. Just looking at the fracture load for each specimen (including those that fractured beyond the base of the beam) in Figure 34 shows that every AGR-1 cantilever beam required a higher load to induce fracture than any of the AGR-2 beams. This isn't by any means a large enough sample size to render any definite conclusions. However, this divergence in mechanical properties does fall in line with data found during nanoindentation testing so far. Since it has been recognized in the nanoindentation testing that mechanical properties within the buffer evolve throughout the coating, measurements of the flexural strengths at similar depths into the coating will be required between the two irradiation experiments for a more direct comparison. This proves to be troublesome as the beams have shown to break at various locations without the use of notches. The beams that showed the most in common in terms of their fracture characteristics were cantilever A from AGR-1 variant 3 and cantilever E from AGR-2, both of which fractured at their base 21.0 µm and 18.5 µm away from the boundary respectively. Cantilever A in this case fractured at around 302 MPa where cantilever E fractured at approximately 184 MPa. Again, a larger data set will be required before any conclusions can be made, but the findings add to a picture showing that there are likely distinctions in the characteristics between AGR-1 and AGR-2 coatings. More data determining the flexural strength as a function of distance from the boundary will require either a sizable number of test specimens or a way to induce fracture at a specific location, such as with the notched specimens.

4.3 Porosity Image Analysis

A total of four mounts consisting of particles from AGR-1 baseline, AGR-1 variant 1, AGR-1 variant 3, and AGR-2 were imaged and processed through Matlab. Seventeen particles were imaged from the baseline particles, fifteen particles from variant 1, fifteen particles from variant 3, and nineteen from AGR-

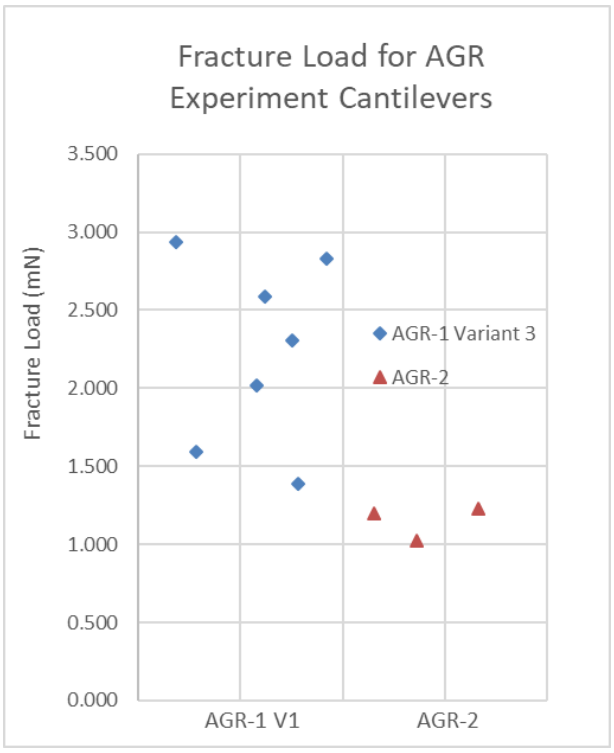


Figure 34: Shows the load required to induce fracture for each of the micro-cantilever beams produced from AGR-1 variant 3 and AGR-2 coatings.

2. The disparity in the number of particles imaged comes from avoiding imaging particles that show damage to the coating from previously run nanoindentation tests. While the coatings on a few of the particles were not always circular and therefore did not exactly match the boundary line overlay as shown in Figure 35, the boundary line generally fit within a few microns of the actual boundary of the IPyC and buffer. The bar graphs produced from the image processing showed sudden increases and decreases in buffer porosity as a function of distance from the boundary, resulting in several local maxima and minima in terms of porosity within each band.

The bar graphs produced from the image processing suggest that local regions of increased porosity exist within the buffer to varying degrees. These regions can vary widely in their overall porosity percentage, the width of the grouping, and the total number of groups within each plot. These features can be denoted within the bar graphs by the peak porosity percentage values, the width of each local maximum region, and the number of local maxima. The purpose of these experiments is to find differences between AGR-1 and AGR-2 coatings, therefore, some metric within the bar graphs must be found by which to compare the two irradiation experiments. Four bar graphs displaying the evolving porosity as a function of radial distance from the boundary can be found in Figure 36, all of which contain peaks that correspond to porous striations in the buffer. One metric to compare the two irradiation experiments would be examining the total porosity percentage of each particle within the region analyzed using the data gathered from imaging (the 60 μm thick region of the buffer that is adjacent to the IPyC). Along with this metric, the 1-micron bands with the highest level of porosity in the particle can be extracted and compared against one another as regions with higher porosity would theoretically show more susceptibility to fracture.

To find any discrepancy in the overall porosity between the irradiation experiments, all of the pixels listed as pores in the 60 μm region of the buffer adjacent to the boundary had been totaled for each particle. These values had then been divided by the total number of pixels in the same 60 μm region to find what percentage of the buffer would be considered porous based on this 2-dimensional imaging of the coatings. For AGR-1 baseline particles the mean overall porosity for this region of the buffer came out at 13.2% with a standard deviation of 3.1%. Particles from AGR-1 variant 1 and 3 appeared to show comparable results averaging out at 12.4% with a standard deviation of 1.8% for variant 1 particles and 12.0% with a standard deviation of 2.5% for variant 3 particles. Results from the imaging of AGR-2 particles on the other hand exhibited distinct measurements from its AGR-1 counterparts. The average overall porosity percentage for AGR-2 particles was determined to be 28.5% with a standard deviation of 7.2%. So, while there is more variation in the AGR-2 buffer coatings, they tend to exhibit an appreciable increase in porosity in the given data set compared to AGR-1 particles. This finding would support the hypothesis that a discrepancy exists between AGR-1 and AGR-2 buffer

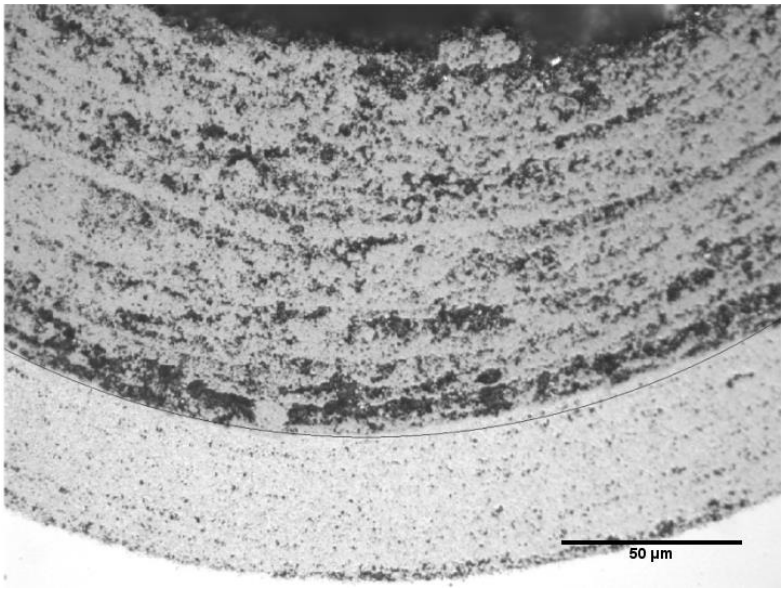


Figure 35: An image of a TRISO particle's buffer and IPyC boundary. The porosity imaging code uses three points along this boundary to auto-populate a line assuming the boundary is perfectly circular, but as can be seen this is not always the case.

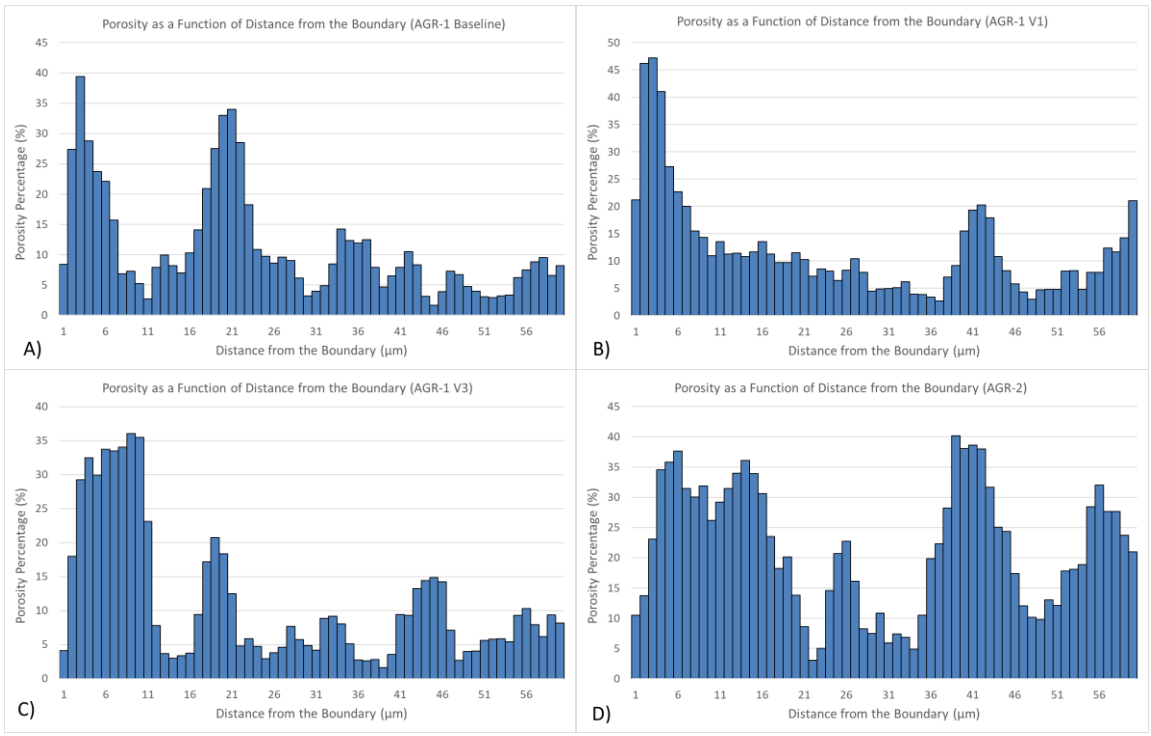


Figure 36: Above shows four separate bar graphs produced from four different TRISO particles subjected to image processing to determine the percentage of porosity found at various distances from the IPyC/buffer boundary.

properties resulting in varied fuel performance as more porosity in AGR-2 particles could very well contribute to the likelihood of the buffer tearing away from the IPyC during irradiation testing. This variation in the porosity found between the two irradiation experiments could be the root cause for the variation found in the nanoindentation and micro-cantilever results as a more porous medium would contribute to the lower hardness and flexural strengths found in AGR-2 buffer coatings. As mentioned in section 4.1, this relationship between porosity, hardness, and flexural strength comes from the voids created by increasing porosity. Increasing porosity results in less material to resist the deformation forces from indentation resulting in a lower hardness with increased porosity. It also results in more stress concentrations within the material and less surface area to distribute forces across that leads to higher stresses. While the pyrolytic carbon itself may have the same strength for AGR-1 and AGR-2, the increased porosity found in AGR-2 particles would result in higher stresses during mechanical tests and would therefore register as having a lower bulk strength compared to that of AGR-1, which was found during micro-cantilever testing. This increase in buffer porosity from AGR-1 to AGR-2 also corresponds to a decrease in buffer density from AGR-1 (1.10 g/cm^3) to AGR-2 (0.99g/cm^3). However, as these values are less than half of the theoretical density of graphite (2.26 g/cm^3) and the overall porosity measurements are in the 10 to 30% range on average for either irradiation experiment, it is obvious that the porosity at the scale being measured is not the only factor in the coating density. Nano-scale porosity or the imperfect nature of pyrolytic carbon mentioned in section 2.1 may also be contributing to the lower density than expected given this porosity data. A 2-dimensional imaging of the pores may also not be an accurate representation of the 3-dimensional porosity characteristics.

Next, the bands containing the highest percentage of porosity in each particle were tabulated along with their location within the buffer in Table 5. Empty cells in this table denote particles that could not be readily imaged. As can be seen from the table, the average porosity value for the most porous bands remained similar for all AGR-1 variants at around 40%. The locations of said bands are also comparable with almost all of the most porous bands being located within the first 10µm of the buffer adjacent to the boundary and all except one particle (particle six of AGR-1 baseline) within 15µm of it. Particle six of the AGR-1 baseline does, however, have a peak within the first ten microns of the boundary similar to that of its maximum porosity value. Comparing these results to the data gathered from imaging AGR-2 particles, variations between the two irradiation experiments can again be discerned. AGR-2 particles were found to have much higher peak porosity values with the bands averaging at around 60% porous. Particles from AGR-2 also showed a greater variation in the location of these peak porosity bands within the buffer as the average location comes out to be approximately 14µm from the boundary with the bulk of the locations ranging from around 4-20 µm away from the boundary. However, all the particles with their maximum porosity band located outside of the first 10 µm, do have a local

Table 5: This table shows the highest porosity percentage band of each particle imaged and the corresponding distance from the boundary within the buffer. The location values refer to the full 1 µm thick band preceding the given value (i.e. 3 refers to all pixels 2-3 µm away from the boundary).

	AGR-1 Baseline		AGR-1 Variant 1		AGR-1 Variant 3		AGR-2	
Particle #	Max Poro. (%)	Dist (µm)	Max Poro. (%)	Dist (µm)	Max Poro. (%)	Dist (µm)	Max Poro. (%)	Dist (µm)
1							40.15	39
2							68.08	9
3	39.43	3					81.16	8
4	34.55	3			36.02	9	61.33	11
5	33.34	6	47.19	3	38.07	6	50.15	4
6	30.46	48	34.40	4	38.68	7	73.00	8
7	49.76	7	38.23	2	42.64	9	59.06	20
8	31.27	11	43.59	10	34.23	10	26.78	18
9	57.03	8	26.70	7	33.66	5	33.97	21
10	54.86	7	46.41	3	44.69	6	79.77	12
11	32.91	4	43.88	5	41.62	7	69.63	5
12	55.11	7	32.71	3	34.71	7	58.64	17
13	43.92	4	57.41	5	47.25	6	58.75	18
14	54.37	9	36.67	2	35.77	4	55.36	18
15	33.31	2	29.19	6	64.07	9	78.33	29
16	26.20	10	45.01	5	39.24	2	58.66	14
17	43.82	5	40.35	7			55.98	8
18	39.26	4	41.67	6	38.95	8	59.87	4
19	50.19	5	26.30	2	29.69	13	72.96	6
Mean:	41.75	8	39.31	5	39.95	7	60.09	14

maximum near or within the first 10μm of the boundary much like the AGR-1 particles imaging showed. This contrast in peak porosity values could also help to understand the difference between AGR-1 and AGR-2 fuel performance as these peak porosity bands are the most likely path for a tear to propagate along. This is supported by the fact that tearing of the buffer during irradiation testing often occurred within the first 10 or so microns of the buffer adjacent to the boundary based on images taken from AGR-1 compacts during PIE, which is within the same region many of these peak porosity bands are located. Therefore, an increase in peak porosity near the boundary of AGR-2 particles could have allowed for a more optimal path for tearing of the buffer to occur during buffer shrinkage preventing the crack from travelling into the IPyC and exposing the SiC.

To show that porosity and hardness are related in the manner mentioned in section 4.1, porosity data was plotted alongside the moving average hardness data as a function of distance from the boundary. This process was performed on every particle where imaging and nanoindentation were implemented in the same location. The results are subjective and, in some cases, inconsistent, but in general the porosity and hardness seem to have an inversely proportional relationship as suspected. One of the better cases demonstrating this interrelationship is shown in Figure 37. In this plot the porosity and indentation data seem to clearly show this inversely proportional relationship up until approximately 45 μm away from the boundary. This may be due to the fact that indentations made farther from the boundary don't having the closest possible point to the boundary within frame, skewing indentation location data at these extended distances. However, not all of the plots showed a clear relationship between the data such as that shown in Figure 38. In this plot it can be observed that the changes in the porosity may have some effect on the hardness, but this effect is not quite as consistent or drastic as it was in Figure 37. A few reasons may exist for this discrepancy with the first being that the porosity imaging simply gathers more data points. Since the imaging process gathers data for each pixel in an image and the images cover a wider area than the nanoindentation arrays in general, the porosity analysis is inherently collecting data outside of the nanoindenter's sampling region. On the other hand, the nanoindentations may be detecting changes in the nano-scale porosity of the carbon or substructure of the carbon below the surface that the imaging process is incapable of detecting.

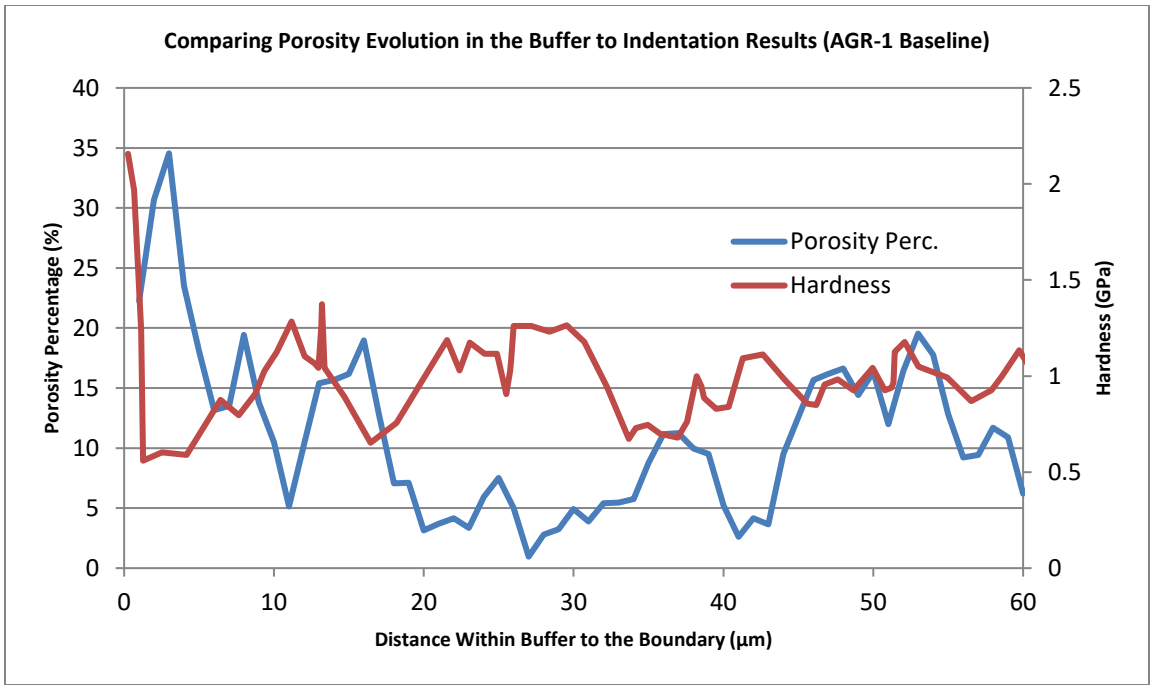


Figure 37: The graph above details the relationship of hardness and porosity within the buffer to the distance from the boundary for an AGR-1 baseline particle.

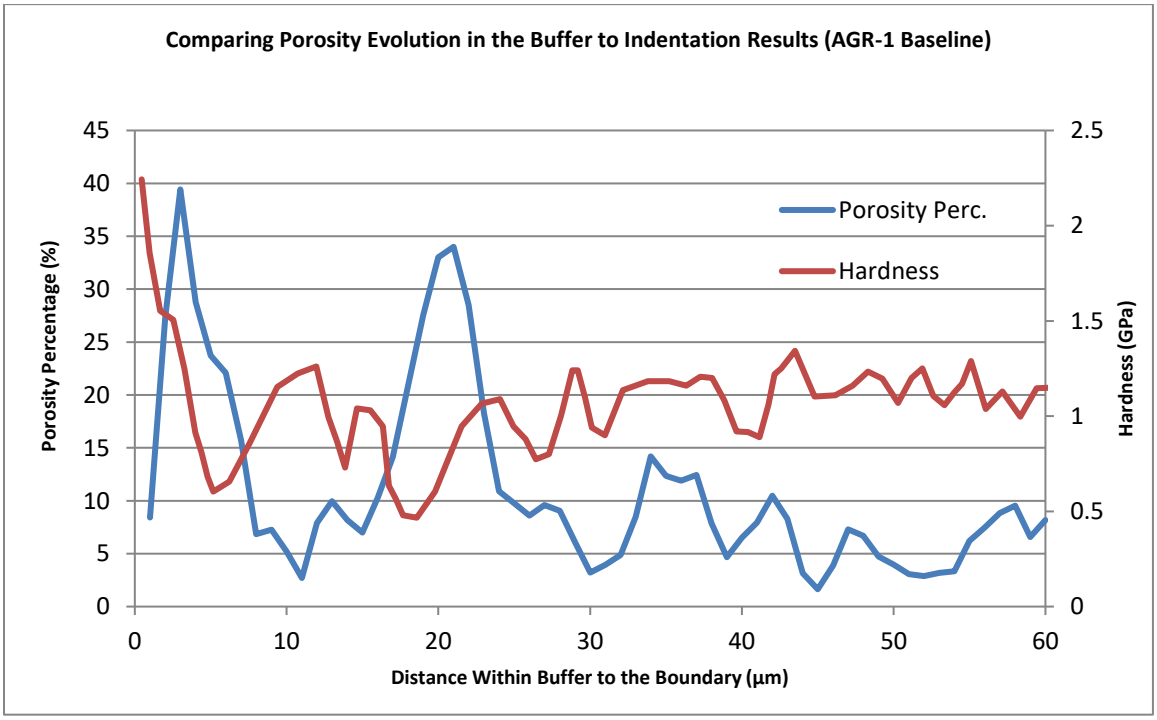


Figure 38: The graph above details the relationship of hardness and porosity within the buffer to the distance from the boundary for an AGR-1 baseline particle.

CHAPTER FIVE

CONCLUSIONS AND RECOMMENDATIONS

Fuel particles from AGR-1 and AGR-2 have shown discrepancies in the frequency of failed particle coatings during PIE. An important factor in this discrepancy seems to be prevalence of the cracks in the IPyC, exposing the main structural component of the fuel, the SiC layer, to deleterious metallic fission products. This fracturing of the IPyC occurs when the buffer densifies under irradiation testing and attempts to pull away from the IPyC. This causes tearing in the buffer adjacent to the IPyC/buffer boundary and typically travels circumferentially around the particle through the buffer. However, in some cases the tear in the buffer would propagate into the IPyC, which was a more common occurrence for AGR-1 particles. Therefore, a desire exists to characterize any differences that may exist between the two sets of coatings.

Several methods have been explored for characterizing primarily the buffer coating as its mechanical properties are suspected to be the culprit of the disparity between the two irradiation experiments. In the end, three methods were chosen for testing. Nanoindentation was chosen as the first method for its ability to quickly probe mechanical properties, micro-cantilever beam testing was chosen for its ability to measure the strength of a specimen in tension, and finally image analysis of the coatings was added for its ability to gather information on the porosity of the buffer with the highest sample throughput. Tensile testing was originally within the scope of work, however, the applied methods for testing proved impractical. The buffer was characterized as a whole and as a function of distance from the buffer/IPyC boundary seeing as the coating primarily tore within 0-10 µm of the boundary.

The nanoindentation results showed promising findings in determining that some level of difference exists in the mechanical properties between AGR-1 and AGR-2 buffer coatings. The buffer in particles from AGR-2 in general showed a lower hardness than those of AGR-1 along with a lower minimum hardness in the region adjacent to the boundary. Micro-cantilever testing also showed that the flexural strength of specimens produced from AGR-2 coatings was lower on average than those of AGR-1 coatings. For this method, however, a larger sample size will be required as only eight specimens were created and fractured under similar conditions. Image analysis of the porosity showed the clearest divergence in properties as AGR-2 buffer coatings exhibited a significant increase in both overall porosity and localized maximum porosity compared to all AGR-1 baseline and variant buffer coatings. The findings in these experiments lay the foundation work for future research into the characterization of these coatings and the capabilities and limitations for each method. Eventually work on this topic may lead to a standardized pass/fail criterion for characterizing coatings in future fuel qualification testing.

Since this is the first attempt at characterizing the buffer and IPyC coatings for this purpose and many of the methods performed are quite novel in their execution, there are a few modifications that could be made moving forward to optimize the processes. First and foremost, a conical tip will be used for future indentation tests based on the results found in section 4.1. As for micro-cantilever testing, a decision will have to be made to determine whether or not to carry on with producing notched specimens, as they allow for controllable fracture locations. On the other hand, it complicates stress calculations and it is unclear how porosity would affect fracture toughness calculations. All methods will, however, require modifications to the methods and equipment used if these tests are to be utilized at industrial-scale quality control efforts in the qualification of fuel coatings.

In short, these methods for characterizing the mechanical properties and porosity of particle fuel have given a glimpse into the differences that exist between AGR-1 and AGR-2 particle coatings. The next step is to refine the testing methods as discussed previously and to continue testing additional particles to find if the trends found in this study are still evident with a larger sample size. If these trends hold up to scrutiny, this would then beg the question “What is causing this discrepancy in coating properties between the two irradiation experiments? “. As mentioned in section 1.4, the longer fluidization times between coating depositions is believed to play a factor in these findings, however, no research into this claim has been performed. So, the next step in this process would be to test this claim and any others (such as variations in irradiation conditions) that are suspected to influence coating properties by implementing a surrogate coating fuel campaign that would test the effects of these variables.

LIST OF REFERENCES

Ando, M., H. Tanigawa, H. Kurotaki and Y. Katoh (2018). "Mechanical properties of neutron irradiated F82H using micro-tensile testing." Nuclear Materials and Energy **16**: 258-262.
Armstrong, D. E. J., C. D. Hardie, J. S. K. L. Gibson, A. J. Bushby, P. D. Edmondson and S. G. Roberts (2015). "Small-scale characterisation of irradiated nuclear materials: Part II nanoindentation and micro-cantilever testing of ion irradiated nuclear materials." Journal of Nuclear Materials **462**: 374-381.
Arregui-Mena, J. D., P. D. Edmondson, A. A. Campbell and Y. Katoh (2018). "Site specific, high-resolution characterisation of porosity in graphite using FIB-SEM tomography." Journal of Nuclear Materials **511**: 164-173.
Baldwin, C. A., J. D. Hunn, R. N. Morris, F. C. Montgomery, C. M. Silva and P. A. Demkowicz (2014). "First elevated-temperature performance testing of coated particle fuel compacts from the AGR-1 irradiation experiment." Nuclear Engineering and Design **271**: 131-141.
Bari, K., C. Osarinmwian, E. López-Honorato and T. J. Abram (2013). "Characterization of the porosity in TRISO coated fuel particles and its effect on the relative thermal diffusivity." Nuclear Engineering and Design **265**: 668-674.
Barrachin, M., V. Basini, Basak U., Ü. Colak, R. Dubourg, M. A. Feltus and W. J. ...Szymczak (2010). High Temperature Gas Cooled Reactor Fuels and Materials. Vienna, INTERNATIONAL ATOMIC ENERGY AGENCY.
Bellan, C. and J. Dhers (2004). "Evaluation of Young modulus of CVD coatings by different techniques." Thin Solid Films **469-470**: 214-220.
Chen, C., S. Nagao, K. Suganuma, J. Jiu, T. Sugahara, H. Zhang, T. Iwashige, K. Sugiura and K. Tsuruta (2017). "Macroscale and microscale fracture toughness of microporous sintered Ag for applications in power electronic devices." Acta Materialia **129**: 41-51.
Collin, B. P. (2011). AGR-2 Irradiation Experiment Test Plan. United States, Idaho National Laboratory.
Demkowicz, P. (2017). The Advanced Gas Reactor Fuel Development and Qualification Program Overview, Idaho National Laboratory.
Deng, Y. and A. Barnoush (2018). "Hydrogen embrittlement revealed via novel in situ fracture experiments using notched micro-cantilever specimens." Acta Materialia **142**: 236-247.
Di Maio, D. and S. Roberts (2005). Measuring fracture toughness of coatings using focused-ion-beam-machined microbeams.
Fischer-Cripps, A. C. (2011). Nanoindentation, Springer-Verlag New York.
Gross, T. S., N. Timoshchuk, I. I. Tsukrov, R. Piat and B. Reznik (2013). "On the ability of nanoindentation to measure anisotropic elastic constants of pyrolytic carbon." ZAMM - Journal of Applied Mathematics and Mechanics / Zeitschrift für Angewandte Mathematik und Mechanik **93**(5): 301-312.
Grover, S. B. and D. A. Petti (2014). "Status of the NGNP fuel experiment AGR-2 irradiated in the advanced test reactor." Nuclear Engineering and Design **271**: 238-243.

Gussev, M. N., R. H. Howard, K. A. Terrani and K. G. Field (2017). "Sub-size tensile specimen design for in-reactor irradiation and post-irradiation testing." Nuclear Engineering and Design **320**: 298-308.
Handin, J. (1969). "On the Coulomb-Mohr failure criterion." Journal of Geophysical Research **74**(22): 5343-5348.
Helmreich, G. W., J. D. Hunn, J. W. McMurray and D. R. Brown (2018). ENHANCED METHOD FOR ANALYSIS OF INDIVIDUAL UCO KERNEL PHASE FRACTIONS. HTR 2018, Warsaw, Poland.
Hosemann, P., J. N. Martos, D. Frazer, G. Vasudevamurthy, T. S. Byun, J. D. Hunn, B. C. Jolly, K. Terrani and M. Okuniewski (2013). "Mechanical characteristics of SiC coating layer in TRISO fuel particles." Journal of Nuclear Materials **442**(1): 133-142.
Huang, S. H., F. Y. Huang and B. H. Yan (2005). "Fracture strength analysis of micro WC-shaft manufactured by micro-electro-discharge machining." The International Journal of Advanced Manufacturing Technology **26**(1-2): 68-77.
Hunn, J. D., C. A. Baldwin, T. J. Gerczak, F. C. Montgomery, R. N. Morris and C. M. Silva (2014). AGR-1 Irradiated Compacts 5-2-3 and 5-2-1 PIE Report: Evaluation of As-Irradiated Fuel Performance with Leach-Burn-Leach, IMGA, Materialography, and X-ray Tomography, Oak Ridge National Laboratory.
Hunn, J. D., C. A. Baldwin, T. J. Gerczak, F. C. Montgomery, R. N. Morris, C. M. Silva, P. A. Demkowicz, J. M. Harp and S. A. Ploger (2016). "Detection and analysis of particles with failed SiC in AGR-1 fuel compacts." Nuclear Engineering and Design **306**: 36-46.
Hunn, J. D., C. A. Baldwin, F. C. Montgomery, T. J. Gerczak, R. N. Morris, G. W. Helmreich, P. A. Demkowicz, J. M. Harp and J. D. Stempien (2018). "Initial examination of fuel compacts and TRISO particles from the US AGR-2 irradiation test." Nuclear Engineering and Design **329**: 89-101.
Hunn, J. D., R. N. Morris, C. A. Baldwin, F. C. Montgomery, C. G. W. Silva and T. J. Gerczak (2012). AGR-1 Irradiated Compact 6-1-1 PIE Report: Evaluation of As-Irradiated Fuel Performance Using Leach Burn Leach, IMGA, Materialography, and X-ray Tomography, Oak Ridge National Laboratory.
Hunn, J. D., R. N. Morris, C. A. Baldwin, F. C. Montgomery, C. M. Silva and T. J. Gerczak (2013). PIE ON THREE IRRADIATED AGR-1 COMPACTS IN FY2013, Oak Ridge National Laboratory.
Jellison, G. E. and J. D. Hunn (2008). "Optical anisotropy measurements of TRISO nuclear fuel particle cross-sections: The method." Journal of Nuclear Materials **372**(1): 36-44.
Jolly, B. C., T. Lindemer and K. A. Terrani (2015). Triso coating development progress for uranium nitride kernels. United States.
Kurdi, A. and A. K. Basak (2018). "Deformation of electrodeposited gradient Co/Sn multilayered coatings under micro-pillar compression." Engineering Fracture Mechanics **204**: 138-146.
Kwiecińska, B. K. and S. Pusz (2016). "Pyrolytic carbon — Definition, classification and occurrence." International Journal of Coal Geology **163**: 1-7.

L. Knudson, D., G. K Miller, D. Petti and J. T. Maki (2009). PARFUME Theory and Model basis Report.
Leyssale, J. M., J. P. Da Costa, C. Germain, P. Weisbecker and G. L. Vignoles (2012). "Structural features of pyrocarbon atomistic models constructed from transmission electron microscopy images." Carbon **50**(12): 4388-4400.
Li, X. and B. Bhushan (2002). "A review of nanoindentation continuous stiffness measurement technique and its applications." Materials Characterization **48**(1): 11-36.
Lima Neto, I. A., M. A. R. Ceia, R. M. Misságia, G. L. P. Oliveira, V. H. Santos, R. P. R. Paranhos and N. L. Archilha (2018). "Testing and evaluation of 2D/3D digital image analysis methods and inclusion theory for microporosity and S-wave prediction in carbonates." Marine and Petroleum Geology **97**: 592-611.
Liu, D. and P. E. J. Flewitt (2017). "Deformation and fracture of carbonaceous materials using in situ micro-mechanical testing." Carbon **114**: 261-274.
López-Honorato, E., P. J. Meadows, P. Xiao, G. Marsh and T. J. Abram (2008). "Structure and mechanical properties of pyrolytic carbon produced by fluidized bed chemical vapor deposition." Nuclear Engineering and Design **238**(11): 3121-3128.
Lowden, R. A., J. Hunn, S. D. Nunn, A. Kercher, J. R. Price and G. E. Jellison, Jr (2005). Effects of deposition conditions on the properties of pyrolytic carbon deposited in a fluidized bed.
Lowe, T., R. S. Bradley, S. Yue, K. Barii, J. Gelb, N. Rohbeck, J. Turner and P. J. Withers (2015). "Microstructural analysis of TRISO particles using multi-scale X-ray computed tomography." Journal of Nuclear Materials **461**: 29-36.
Maki, J. T. (2009). AGR-1 Irradiation Experiment Test Plan. United States.
Matoy, K., H. Schönherr, T. Detzel, T. Schöberl, R. Pippan, C. Motz and G. Dehm (2009). "A comparative micro-cantilever study of the mechanical behavior of silicon based passivation films." Thin Solid Films **518**(1): 247-256.
Oliver, W. C. and G. M. Pharr (1992). "An improved technique for determining hardness and elastic modulus using load and displacement sensing indentation experiments."
Petti, D., H. Gougar and G. Bell (2005). The DOE Advanced Gas Reactor (AGR) Fuel Development and Qualification Program. United States**:** v.
Petti, D. A., J. Buongiorno, J. T. Maki, R. R. Hobbins and G. K. Miller (2003). "Key differences in the fabrication, irradiation and high temperature accident testing of US and German TRISO-coated particle fuel, and their implications on fuel performance." Nuclear Engineering and Design **222**(2): 281-297.
Phani, K. K. and S. K. Niyogi (1987). "Young's modulus of porous brittle solids." Journal of Materials Science **22**(1): 257-263.
Ploger, S. A., P. A. Demkowicz, J. D. Hunn and J. S. Kehn (2014). "Microscopic analysis of irradiated AGR-1 coated particle fuel compacts." Nuclear Engineering and Design **271**: 221-230.
Reznik, B. and K. J Hüttinger (2002). On the terminology of pyrolytic carbon.

Rice, F. J., J. D. Stempien and P. A. Demkowicz (2018). "Ceramography of irradiated TRISO fuel from the AGR-2 experiment." Nuclear Engineering and Design **329**: 73-81.
Ritchie, R. (1996). Fatigue and fracture of pyrolytic carbon: A damage-tolerant approach to structural integrity and life prediction in "ceramic" heart valve prostheses.
Schiffmann, K. I. (2007). "Area function calibration in nanoindentation using the hardness instead of Young's modulus of fused silica as a reference value." International Journal of Materials Research **98**(5): 424-429.
Shih, C., Y. Katoh, K. J. Leonard, H. Bei and E. Lara-Curzio (2013). "Determination of interfacial mechanical properties of ceramic composites by the compression of micro-pillar test specimens." Journal of Materials Science **48**(15): 5219-5224.
Spierings, A. B., M. Schneider and R. Eggenberger (2011). "Comparison of density measurement techniques for additive manufactured metallic parts." Rapid Prototyping Journal **17**(5): 380-386.
Uchic, M. D. and D. M. Dimiduk (2005). "A methodology to investigate size scale effects in crystalline plasticity using uniaxial compression testing." Materials Science and Engineering: A **400-401**: 268-278.
VanLandingham, M. R., T. F. Juliano and M. J. Hagon (2005). "Measuring tip shape for instrumented indentation using atomic force microscopy." Measurement Science and Technology **16**(11): 2173-2185.
Weihs, T. P., S. Hong, J. C. Bravman and W. D. Nix (2011). "Mechanical deflection of cantilever microbeams: A new technique for testing the mechanical properties of thin films." Journal of Materials Research **3**(5): 931-942.
Yilmaz, E. D., H. Jelitto and G. A. Schneider (2015). "Uniaxial compressive behavior of micro-pillars of dental enamel characterized in multiple directions." Acta Biomaterialia **16**: 187-195.
Žagar, G., V. Pejchal, M. G. Mueller, L. Michelet and A. Mortensen (2016). "Fracture toughness measurement in fused quartz using triangular chevron-notched micro-cantilevers." Scripta Materialia **112**: 132-135.
Zhao, L., Q. Guo, Z. Li, Z. Li, G. Fan, D.-B. Xiong, Y. Su, J. Zhang, Z. Tan and D. Zhang (2018). "Strain-rate dependent deformation mechanism of graphene-Al nanolaminated composites studied using micro-pillar compression." International Journal of Plasticity **105**: 128-140.

VITA

Austin Schumacher was born in the city of Hendersonville, Tennessee just outside of Nashville, Tennessee. He attended high school in the same town at Hendersonville High School until graduating in 2011. He then attended undergraduate studies at the University of Tennessee, Knoxville in the mechanical engineering program. During his time at the university he began a cooperative education program working for Shaw Industries for three semesters. He graduated from the University of Tennessee with his bachelor's degree in spring 2016 and began his graduate studies the following fall. Around the same time, he was hired at the Oak Ridge National Laboratory in the nuclear fuels group as a post-bachelor's research associate. He was the later hired on as a staff member in the material science division in May 2019.